Geol. Mag. **148** (*4*), *2011, pp. 558–579. © Cambridge University Press 2010*
doi:10.1017/S001675681000097X

Fluid flow within the damage zone of the Boccheggiano extensional fault (Larderello–Travale geothermal field, central Italy): structures, alteration and implications for hydrothermal mineralization in extensional settings

FEDERICO ROSSETTI*†, LUCA ALDEGA*‡, FRANCESCA TECCE§, FABRIZIO BALSAMO*, ANDREA BILLI§ &MAURO BRILLI§

*Dipartimento di Scienze Geologiche, Università Roma Tre, 00146 Rome, Italy
‡Dipartimento di Scienze della Terra, Sapienza Università di Roma, 00185 Rome, Italy
§Istituto di Geologia Ambientale e Geoingegneria, CNR, Rome, Italy

(*Received* 23 April 2010; *accepted* 22 September 2010; *first published online* 22 December 2010)

Abstract – The Neogene extensional province of southern Tuscany in central Italy provides an outstanding example of fossil and active structurally controlled fluid flow and epithermal ore mineralization associated with post-orogenic silicic magmatism. Characterization of the hydrodynamic regime leading to the genesis of the polysulphide deposit (known as Filone di Boccheggiano) hosted within the damage zone of the Boccheggiano Fault is a key target to assess modes of fossil hydrothermal fluid circulation in the region and, more generally, to provide inferences on fault-controlled hydrothermal fluid flow in extensional settings. We provide a detailed description of the fault zone architecture and alteration/mineralization associated with the Boccheggiano ore deposit and report the results of fluid inclusion and stable oxygen isotope studies. This investigation shows that the Boccheggiano ore consists of an adularia/illite-type epithermal deposit and that sulphide ore deposition was controlled by channelling of hydrothermal fluids of dominantly meteoric origin within the highly anisotropic permeability structure of the Boccheggiano Fault. The low permeability structure of the fault core compartmentalized the fluid outflow preventing substantial cross-fault flow, with focused fluid flow occurring at the hangingwall of the fault controlled by fracture permeability. Fluid inclusion characteristics indicate that ore minerals were deposited between 280° and 350 °C in the upper levels of the brittle extending crust (lithostatic pressure in the order of 0.1 GPa). Abundant vapour-rich inclusions in ore-stage quartz are consistent with fluid immiscibility and boiling, and quartz ore vein textures suggest that mineralization in the Boccheggiano ore deposit occurred during cyclic fluid flow in a deformation regime regulated by transient and fluctuating fluid pressure conditions. Results from this study (i) predict a strongly anisotropic permeability structure of the fault damage zone during crustal extension, and (ii) indicate the rate of secondary (structural) permeability creation and maintenance by active deformation in the hangingwall of extensional faults as the major factor leading to effective hydraulic transmissivity in extensional terranes. These features intimately link ore-grade mineralization in extensional settings to telescoping of hydrothermal flow along the hangingwall block(s) of major extensional fault zones.

Keywords: fluid flow, hydrothermal mineralization, alteration, fracture permeability, extensional faulting, Larderello geothermal field, Italy.

1. Introduction

The hydrodynamic regime in hydrothermal systems is dominated by advective fluid flow at shallow crustal levels, controlled by thermal/chemical buoyancy-driven convective circulation under a cold/hot hydrostatic fluid pressure regime (e.g. Henley, 1985; Hedenquist & Lowenstern, 1994; Hanson, 1995). Permeability distribution within the rock mass primarily controls the mode of hydrothermal flow, which is typically focused along large-scale, structurally controlled zones of high permeability (e.g. Oliver, 1996; Sibson, 1996; Cartwright & Buick, 1999; Cox, Knackstedt & Braun, 2001). Evidence from active and fossil hydrothermal systems indicates, in particular, that faulting of the brittle crust exerts a primary role in providing fracture-controlled, high-permeability conduits that focus fluid flow (e.g. Curewitz & Karson, 1997). As such, fluid discharge along fracture-controlled fluid pathways has a significant role in genesis of epithermal ore deposits and associated alteration zones (e.g. Henley, 1985; Sibson, 1987; Dipple & Ferry, 1992; Cox, Knackstedt & Braun, 2001; Sheldon & Ord, 2005). Structural permeability induced by faulting is intrinsically anisotropic in time and space owing to a range of possible fault zone architecture varying with displacement, host rock lithology and fault rock cementation (e.g. Caine, Evans & Forster, 1996; Rowland & Sibson, 2004). Active deformation (fracturing) is a necessary prerequisite

†Author for correspondence: rossetti@uniroma3.it

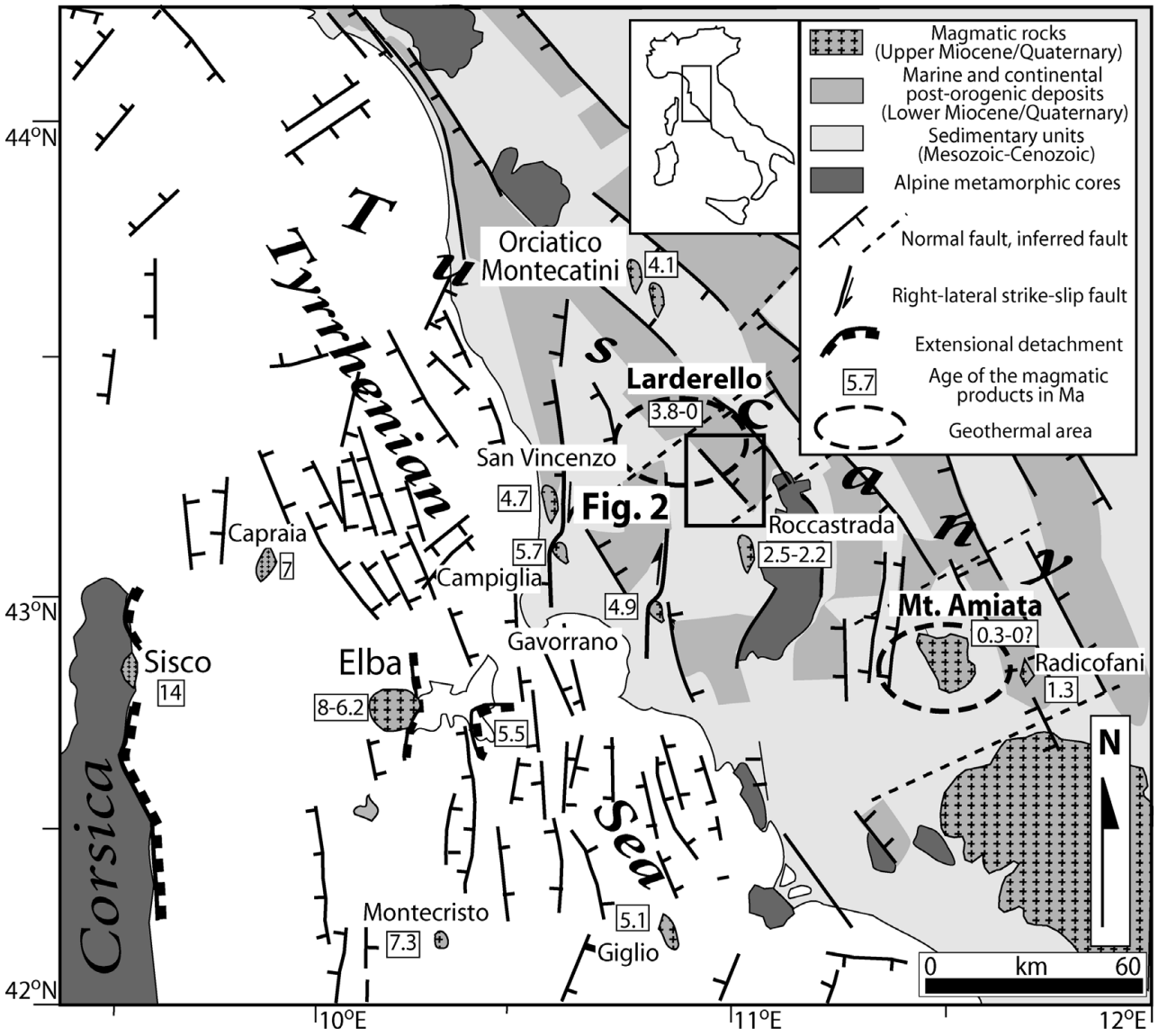

Figure 1. Regional geological map of the Tuscan region with location of the study area (modified and readapted after Jolivet *et al*. 1998). The map also illustrates distribution and age of post-orogenic magmatism (after Dini *et al*. 2002).

to maintain structural permeability and to sustain fluid flow in hydrothermal systems that should be instead inhibited by rapid mineral precipitation in the permeable pathways (e.g. Sibson, 1987, 1996; Cox, Knackstedt & Braun, 2001).

Hydrothermal activity commonly occurs in regions of active tectonism associated with magmatism, where the geological structure hosts a geothermal system and input of magmatic heat promotes structurally controlled, near-surface convective upflow, fluid–rock interaction and dispersion (Henley, 1985). The Neogene extensional domain of southern Tuscany in central Italy (Fig. 1) provides an outstanding example of both fossil and active magma-related hydrothermal systems, as attested by diffuse distribution of epithermal ore deposits, mineralized hot springs and active geothermal systems (e.g. Arisi Rota & Vighi, 1971; Tanelli, 1983; Lattanzi, 1999; Batini *et al*. 2003; Dini, 2003; Bellani *et al*. 2004; Liotta *et al*. 2009). In particular, a long-lived thermal anomaly focused by advection of heat driven by multiple granite emplacements during the last 3.8 Ma is recorded in the Larderello–Travale geothermal region (Gianelli, Manzella & Puxeddu, 1997; Mongelli, Pialli & Zito, 1998; Dini *et al*. 2005; Villa *et al*. 2006; Bertini *et al*. 2006; Boiron *et al*. 2007; Rossetti *et al*. 2008). This is the area with the largest geothermal anomaly in Italy, with a maximum thermal heat flow of more than 600 mW m^{-2} (Mongelli, Pialli & Zito, 1998). The intimate relationships between ore deposits and active hydrothermal systems, coupled with the wealth of both geological and geophysical data acquired during geothermal exploratory activities, make the Larderello–Travale geothermal area a key region to investigate modes of hydrothermal flow (see for example Cavarretta, Gianelli & Puxeddu, 1982; Cathelineau *et al*. 1994; Ruggieri *et al*. 1999; Ruggieri & Gianelli, 1999; Boyce, Fulignati & Sbrana, 2003). Recent investigations have elucidated fault patterns and their extensional kinematics (e.g. Brogi *et al*. 2003; Rossetti *et al*. 2008) and have addressed the issue of

https://doi.org/10.1017/S001675681000097X Published online by Cambridge University Press

the structural control on fluid circulation in the region (Bellani *et al*. 2004; Liotta *et al*. 2009), providing a basis for formulation of the hydrological modelling of the past and present geothermal reservoir.

This study describes modes of fluid flow, fluid–rock interaction and alteration mineralogy within the damage zone of the Pliocene Boccheggiano extensional fault (hereafter referred to as BF; Fig. 2), which has been recognized as the main hydraulic channel for hydrothermal circulation in the southern branch of the Larderello geothermal field (Liotta *et al*. 2009). The findings of this study are used (i) to propose a hydrodynamic model for fluid flow and mineralization within the damage zone of the BF, and (ii) to infer possible implications for the modalities of fault-controlled hydrothermal outflow in extensional settings.

2. Regional geology and the Boccheggiano mining area

The Larderello–Travale geothermal field covers an area of about 400 km^2 and consists of a steam-heated reservoir (temperature of 200–350 °C at a pressure of 4–7 MPa) with 28 power units for a total installed capacity of 703 MWe (Bertani, 2005). Available drillhole logs and geophysical and seismic data have documented that the metamorphic substratum is pervasively intruded by granitic intrusions that, together with the associated alteration caps and contact aureoles, were found at relatively shallow depth (from about 2000 m below ground level; Franceschini, 1998; Boyce, Fulignati & Sbrana, 2003; Dini *et al*. 2005; Villa *et al*. 2006; Bertini *et al*. 2006; Rossetti *et al*. 2008). This is the evidence of a regional-sized (at least 300 km^2) intrusive complex that evolved from multiple magmatic pulses from about 3.8 to 0.7 Ma to form a major tabular granitic intrusion (Bertini *et al*. 2006; Rossetti *et al*. 2008).

Neogene extensional faulting controls localization and distribution of epithermal ore-grade sulphide mineralization (Arisi Rota & Vighi, 1971; Tanelli, 1983). Among these, the polymetallic sulphide (Cu–Pb–Zn) deposit hosted within the damage zone of the BF constitutes by far the most important mining site for pyrite exploitation in the region, which lasted beyond the 1990s in the Campiano Mine (Fig. 2). The BF constitutes the eastern boundary of the Boccheggiano tectonic window, where the low-grade metamorphic sequences of the Tuscan Metamorphic Complex (TMC; Boccheggiano Fm) crop out (Costantini *et al*. 2002) (Fig. 2). Pyrite ores occur both as sub-horizontal conformable bodies within the Boccheggiano Fm at the footwall of the BF and as veins and masses localized at the immediate hangingwall (Masotti & Favilli, 1987) (see inset in Fig. 2). Sulphide mineral assemblages consist of pyrite–sphalerite, galena, chalcopyrite and tetrahedrite in association with Fe oxides and native Ag (Masotti & Favilli, 1987; Corsini, Morelli & Tanelli, 1991), which are typical of intermediate-sulphidation epithermal deposits (Einaudi, Hedenquist & Inan, 2003). The temperature of ore forming fluids was between 290 and 375 °C, and the elemental and isotopic compositions of the Campiano sulphide deposits suggest that the sulphur was likely a mixture of magmatic and inorganic sources (Cortecci, Lattanzi & Tanelli, 1985; Martarelli, Ferrini & Masi, 1995).

The LAR-46 seismic reflection profile (acquired by ENEL Green Power Electric Company for geothermal exploration purposes) provides information on both the subsurface prolongation of the BF and the lithostratigraphic and structural architecture of the Boccheggiano mining area (Rossetti *et al*. 2008; Liotta *et al*. 2009). The subsurface prolongation of the BF is well imaged as a set of sinuous low-angle reflections down to about 0.5 s TWT (two-way time), corresponding to a depth of about 1 km (see also Brogi *et al*. 2003). The seismic expression of the BF fades at the top of the *c*. 3 Ma Montieri pluton of Villa *et al*. (2006), whose top surface is well imaged by a set of rather continuous reflections, culminating at the core of the Boccheggiano tectonic window (see the geological cross-section in Fig. 2).

3. Methods

Fluid–rock interactions associated with hydrothermal sulphide ore mineralization along the BF were investigated through an integrated approach that combines structural, mineralogical and geochemical data. Structural investigations were carried out both at the meso- and the micro-scale to define the linkage between faulting and hydrothermal mineralization, as well as the structural architecture across the BF. Patterns and mineralogical changes associated with the mineralized host rocks were defined by means of X-ray diffraction quantitative analyses. The volumes and possible sources for fluids involved in the hydrothermal mineralization were investigated through the application of whole-rock geochemical, fluid inclusion and stable oxygen isotope studies. The analytical methods adopted in this study are described in the Appendix.

4. Fault zone architecture and permeability structure

The BF is a part of the NW–SE-striking, E-dipping extensional fault system that controlled the structural architecture of the southern branch of the Larderello geothermal field during Pliocene–Pleistocene times (Brogi *et al*. 2003; Bellani *et al*. 2005; Rossetti *et al*. 2008; Liotta *et al*. 2009). Normal offset along the BF is estimated in the order of 1800 m (Costantini *et al*. 2002). In the fault footwall, the Palaeozoic phyllites of the Boccheggiano Fm show a sub-horizontal foliation attitude and a main second-phase ductile plano-linear fabric. The fault hangingwall consists of marine siliceous-carbonate strata belonging to the Ligurian Complex (Calcari a Palombini Fm), Cretaceous in age. In the immediate hangingwall of the BF, these strata are intensively metasomatized and mineralized to form the major massive sulphide ore deposit known as the Filone di Boccheggiano (Masotti & Favilli, 1987).

https://doi.org/10.1017/S001675681000097X Published online by Cambridge University Press

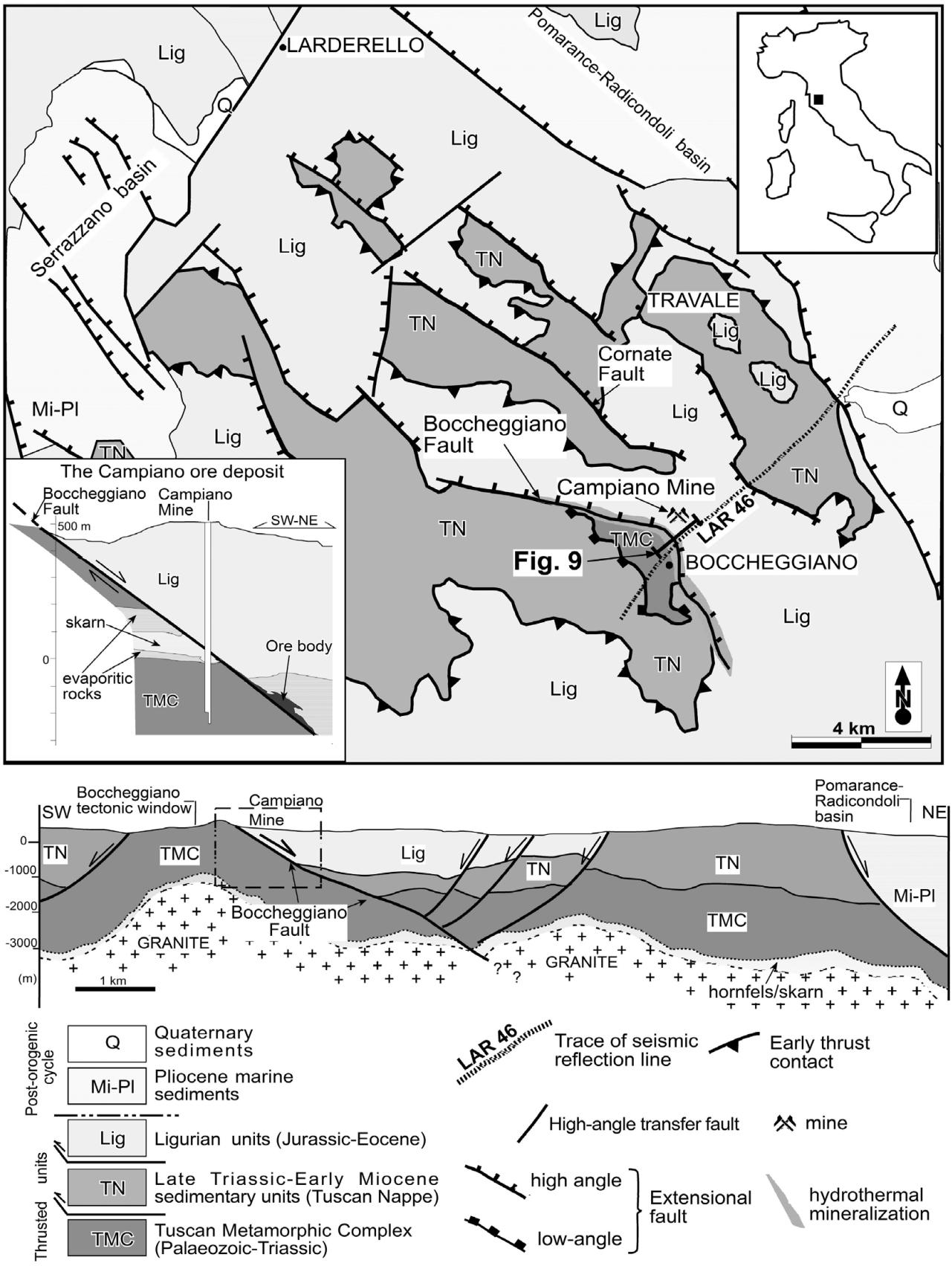

Figure 2. Geology of the Larderello geothermal region (modified and re-adapted after Brogi *et al*. 2003) and the subsurface structural architecture as reconstructed from the LAR46 seismic line. The reflections interpreted as the subsurface prolongation of the Boccheggiano Fault fade into the Montieri pluton whose summit is also known from borehole data (modified and readapted after Rossetti *et al*. 2008). The inset shows the cross-section of the Campiano ore deposit, with location of the main ore deposits (after Masotti & Favilli, 1987).

https://doi.org/10.1017/S001675681000097X Published online by Cambridge University Press

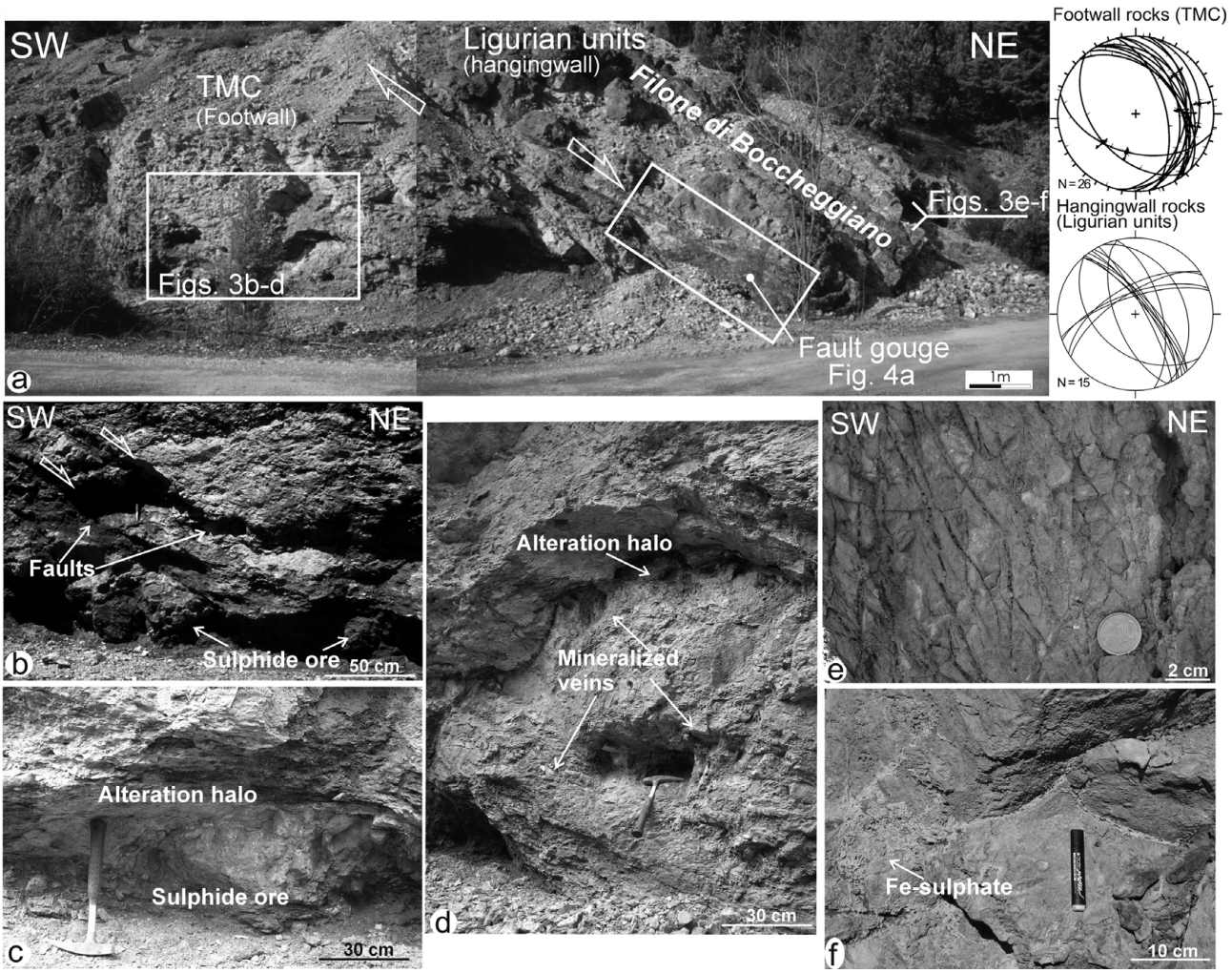

Figure 3. (a) Studied exposure of the Boccheggiano Fault. The main ore deposit (Filone di Boccheggiano) is located in the immediate hangingwall of the fault. To the left: stereographic projections (Schmidt equal-area net, lower hemisphere) of representative structural data collected within the damage zone of the BF: (top) fault planes with slickenlines at the footwall of the fault (TMC); (bottom) fracture planes at the fault hangingwall. Fault and fracture planes as great circles; slickenlines as arrows. (b) Sub-horizontal quartz-sulphide breccia veins in the TMC at footwall of the BF. Note that extensional faults cut across the veins. (c) Enlargement of (b) showing the alteration halos surrounding the veins. (d) Sub-horizontal quartz veins and associated mineral alteration at the footwall of the BF. Note the sub-horizontal attitude of foliation in the TMC rocks. (e) Brittle tectonic fabric (fault fracture meshes) in the immediate hangingwall of the BF (i.e. about 5 m from the principal fault surface). (f) Sulphate mineralization decorating the fracture systems within the damage zone of the BF. See http://journals.cambridge.org/geo for a colour version of this figure.

Along the fault, the carbonate strata strike N140° and dip towards the northeast by about 25° (see also Costantini *et al*. 2002).

Field studies have documented that the BF consists of two nearly parallel, low-angle NW–SE-striking extensional fault strands, linked by a N–S-striking, high-angle dextral fault segment (Rossetti *et al*. 2008) (Fig. 2). The damage zone thickness varies across strike (from about 20 to 100 m across both the footwall and the hangingwall), broadening within the N–S-striking fault zone. Within the fault damage zone, the fracture pattern consists of steeply dipping, seldom conjugated joints striking nearly subparallel to the strike of the main fault segments, i.e. NW–SE and N–S. Both the footwall and the hangingwall rocks included in the fault damage zone underwent intense metasomatic alteration during hydrothermal fluid flow and sulphide ore deposition. Alteration mostly obliterated the original (primary and secondary) rock fabrics, which are preserved only in a few outcrops. The fault rocks include a *c*. 30 m thick damage zone, which encloses a *c*. 1 m thick fault core (Fig. 3a). Rock fabric in the damage zone is distinctly different when moving from the footwall to the hangingwall of the fault. Footwall rocks are affected by a set of low-angle (average dip 40°), E-dipping anastomosing extensional fault systems synthetic to the shear transport direction of the BF (Fig. 3a, b). Sub-horizontal, foliation-parallel, quartz-sulphide vein (1–2 to 50 cm across) arrays and breccia bodies also occur within the footwall rocks and are cut across by the E-dipping fault systems (Fig. 3c, d). In the fault hangingwall, exposed rocks show a massive aspect and the fabric is dominated by a conjugate set of high-angle, closely spaced joints and veins with apertures between about 0.1 and 3 mm (Fig. 3e). Attitude and aperture

https://doi.org/10.1017/S001675681000097X Published online by Cambridge University Press

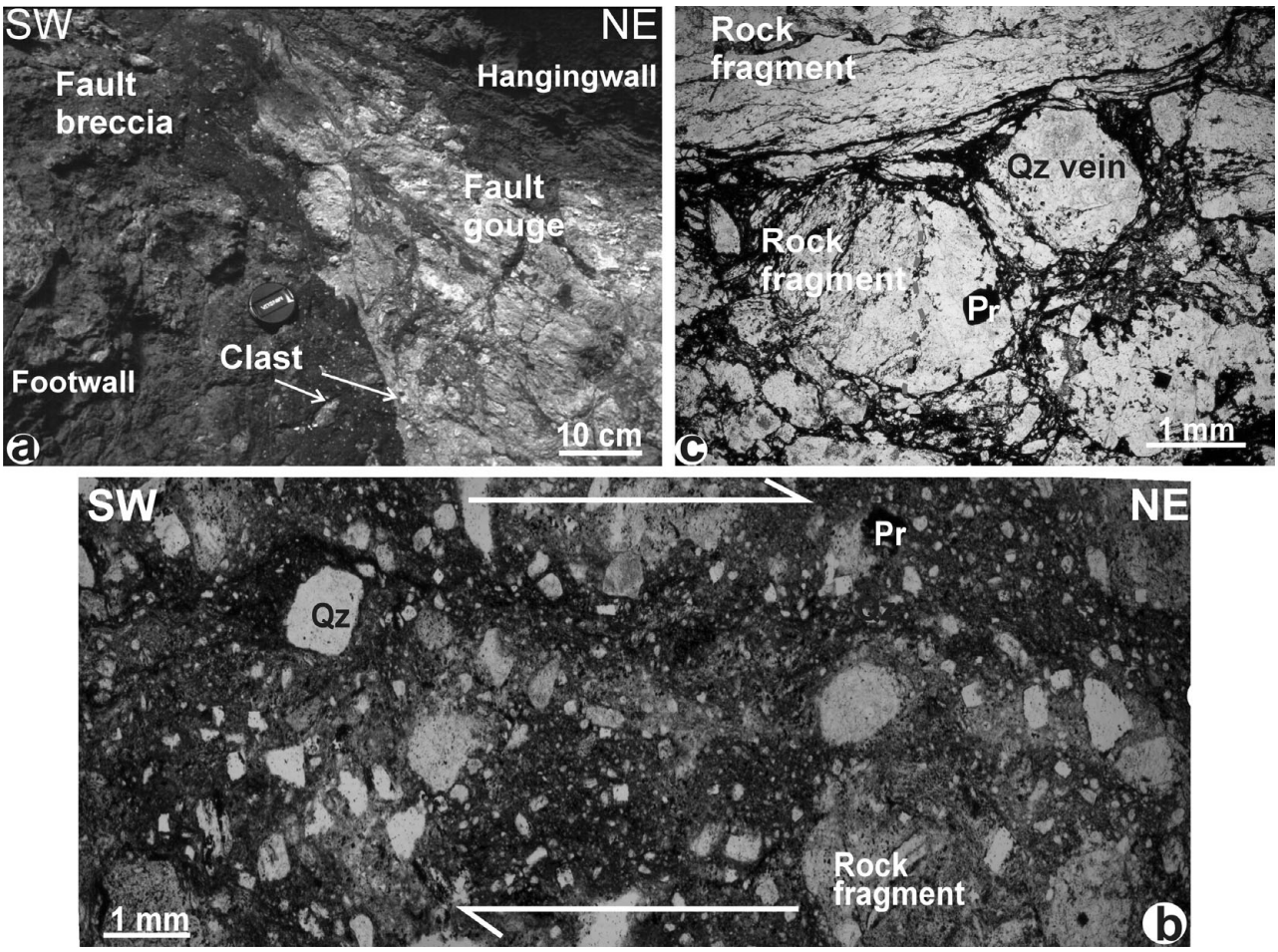

Figure 4. (a) The fault core of the Boccheggiano Fault. Transition from a cohesive fault breccia to a fine-grained fault gouge is observed. (b) Thin-section microphotograph of the fault gouge (natural light) showing cataclastic fabric with survivor grains surrounded by a very fine-grained matrix. Contacts among coarse grains are absent or very rare. (c) Thin-section microphotograph of the Boccheggiano Fault breccia showing an early stage of the cataclastic process as inferred from the size of the grains (i.e. significantly larger than those forming the adjacent fault gouge) and from the numerous contacts among the coarse grains. Pr – pyrite; Qz – quartz.

of these joints are kinematically consistent with the fault slip. A subordinate set of joints strikes N50° and dips towards the northwest by about 70° (Fig. 3a). Late sulphate mineralization also occurs across the fault core in both the footwall and hangingwall rocks, permeating the pre-existing fracture pattern (Fig. 3f).

The fault core thickness is variable along the fault and the fault core and includes (i) an inner dark, 60–70 cm thick layer of cohesive foliated phyllosilicate-rich gouge (phyllonite); and (ii) an outer 120–130 cm thick layer of fault breccia (Figs 3a, 4a). Microphotographs obtained from impregnated samples of the fault gouge show that the core consists of a few isolated sub-rounded survivor grains, most of which are less than 1 mm in size (Fig. 4b). These grains, made of fragments of both metamorphic host rock (predominantly composed of white mica and quartz) and quartz-pyrite veins, are embedded within a clayey matrix. The remainder of the phyllonite is made dominantly of quartz microlithons (mostly relict veins) and minor opaques. Pyrite crystals are also disseminated within the phyllonite matrix. The fault breccia consists of angular and coarse grains with a diameter generally larger than 1 mm (Fig. 4c). By using the Optimas 6.51 software for image analysis produced by Media Cybernetics (Silver Spring, Maryland, USA), we determined the size distribution (e.g. Francus, 1998) of the coarse grains as displayed in the differently magnified images shown in Figure 5 (760 × 560 pixels, resolution 253 dpi). For each detected grain, the software semi-automatically computed the diameter (here named equivalent diameter) of a circle with the same area as the grain area. The obtained equivalent diameters are plotted against the relative numbers of data. Results show that the fault gouge consists of some isolated survivor grains, which mainly range in size between 0.063 and 0.032 mm (i.e. sand- to silt-size grains; Fig. 5a). These grains are embedded within a matrix whose grain size mostly spans the fine domain of the clay sizes (Fig. 5b).

To infer information about the hydraulic properties of the fault hangingwall and footwall, we measured the abundance of fractures and the fault-related porosity in the related rocks (i.e. from the fault hangingwall and footwall; see Fig. A1 in the online Appendix at http://journals.cambridge.org/geo).

https://doi.org/10.1017/S001675681000097X Published online by Cambridge University Press

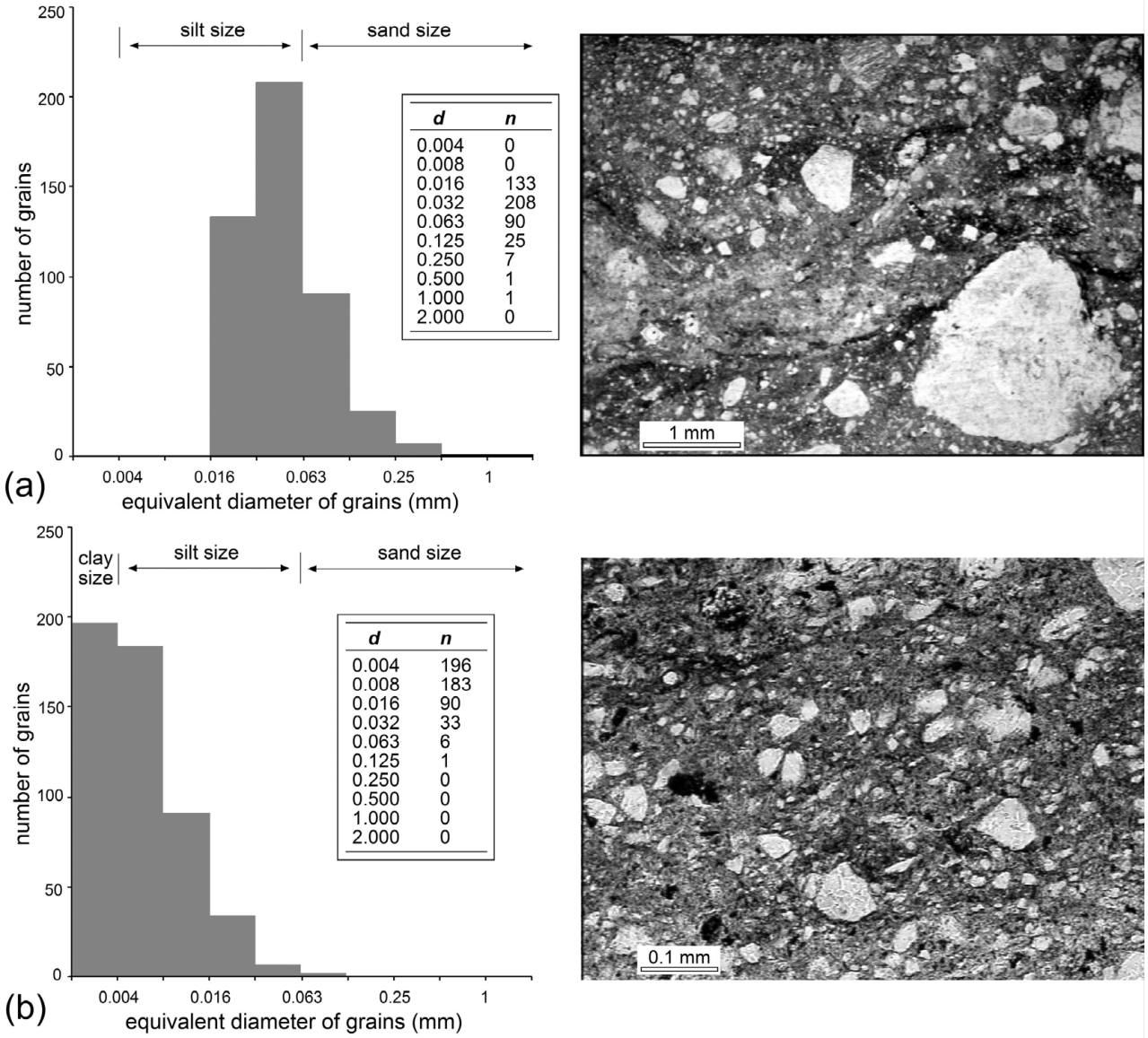

Figure 5. Representative histograms showing the 2D grain size distribution within the fault gouge of the Boccheggiano Fault as determined after the image analyses of microphotographs. The measured grains are only those measurable in the considered photographs (i.e. only the coarsest grains; d – equivalent diameter of grains; n – number of grains). (a) Survivor grains. (b) Matrix grains.

The fracture abundance was determined by the circle-inventory method (Titley, 1976; Davis & Reynolds, 1996). In this method, the fracture abundance (ρ_f) is defined as the total length of all fractures (L) within a significant (i.e. for the fracture abundance) inventory circle of radius r divided by the area of the circle itself, according to the following expression:

$$\rho_f = L/\pi r^2 \quad (1)$$

where ρ_f is measured in units of length/area (hereafter referred to as mm^{-1}). Results are expressed in mm^{-1} and show that the fracture abundance of the fault hangingwall is about three orders of magnitude greater than the fracture abundance from the fault footwall (0.1761 versus 0.0005 mm^{-1}; see Fig. A1 in the online Appendix at http://journals.cambridge.org/geo). The fracture-related porosity was determined by a circle-inventory modified method (Billi *et al*. 2007). Results show that the fracture-related porosity of the fault hangingwall is about one order of magnitude greater than that of the fault footwall (12:2). It should be noted that these porosity values are estimates done on the exposed rocks. The same rocks under different boundary conditions (i.e. in the subsurface) may be characterized by significantly different porosities.

5. Mineralized zones and vein textures

Sulphide mineralization occurs disseminated within the damage zone of the BF, dominantly within quartz vein ore bodies. Distinct structural characteristics are observed when moving from the footwall to the hangingwall of the BF (Fig. 3). In the footwall, mineralized zones are observed for a maximum distance of about 20 m from the fault core, and consist of multi-stage, sub-horizontal quartz-sulphide veins, including

https://doi.org/10.1017/S001675681000097X Published online by Cambridge University Press

breccia veins, up to 50 cm thick (Fig. 3b, c). Veins are largely composed of quartz, but occasionally contain minor adularia, white mica and disseminated sulphide grains. Pale, centimetre to decimetre thick alteration zones are systematically associated with the veins that commonly lie within the fault zones, documenting an overall pre-faulting veining (Fig. 3b, d). Breccia veins form discontinuous pinch and swell massive bodies (Fig. 3b), made of hydrothermally altered TMC angular wall rock and vein fragments supported by a matrix of quartz-sulphide minerals (Fig. 6a, b). Quartz typically exhibits a blocky texture (e.g. Bons, 2000), with multiple episodes of fracture opening and mineral precipitation (crack-sealing/healing processes) (Fig. 6c). Texturally late brecciation and fracturing of the previously sutured intragranular quartz contacts are commonly observed and adularia-pyrite with minor illite segregations commonly constitutes the cement filling the voids (size 50–100 μm) (Fig. 6c, d). The main ore bodies occur in the immediate hangingwall of the BF and are irregular in shape, dominantly controlled by well-developed fault fracture meshes, which formed an interconnected high permeability network (Fig. 3e). Sulphide ore minerals dominantly occur as open-space filling in a strongly altered, highly siliceous, vuggy rock matrix (Fig. 6e). Quartz and adularia are the dominant gangue minerals that make up the vein fill, together with variable amounts of pyrite. Euhedral blocky textures in quartz are common, with well-preserved growth zoning marked by dense arrays of fluid inclusions (Fig. 6f). The size of the quartz crystals in the vein commonly ranges from 0.1 to 2 mm and the pores between quartz crystals are commonly filled by pyrite and anhedral adularia. These textural features are indicative of advective fluid flow regimes (Oliver & Bons, 2001) and argue for high rates of fluid ascent during blocky vein formation (Okamoto & Tsuchiya, 2009).

6. Fluid inclusion data

A fluid inclusion study was carried out on quartz separates from both footwall (F3 samples) and hangingwall (FIL samples) vein quartz ore bodies. Samples were prepared as 200 μm thick, doubly polished sections, then observed with a polarized microscope to define types of fluid inclusions and their genetic relationships, and analysed to study physico-chemical characteristics and origin of the segregating fluid.

6.a. Hangingwall veins (FIL samples)

Two compositional types of fluid inclusions have been detected in euhedral inner quartz crystals from FIL samples: (i) Type-1, three-phase liquid aqueous, liquid carbonic and vapour carbonic ($L_{aq} + L_{car} + V_{car}$), H_2O–CO_2 inclusions, and (ii) Type-2, two-phase liquid and vapour (L + V), L-rich, H_2O–NaCl inclusions (Fig. 7a). Type-1 inclusions are mainly V-rich, with the carbonic volumetric fraction ranging from about 50 to 90 %; CO_2 is nearly equally partitioned between the liquid and gas phases. They occur as isolated clusters or small trails, trapped in the cores of the inner quartz crystals of the veins. Type-2 inclusions occur within the quartz growth zones, but also in association with Type-1 inclusions in the inner cores of the quartz crystals. They also occur as intragranular and intergranular trails (Fig. 7a). No evidence of CO_2 or other gases has been observed in Type-2 fluid inclusions. Type-1 fluid inclusions have dimensions up to 25–30 μm; Type-2 are smaller and their sizes reach 10–15 μm. Based on petrographic observation, Type-1 fluid inclusions are considered the earliest generation, together with the Type-2 ones marking the inner growth zoning domains. Intragranular rows of Type-2 fluid inclusions are instead considered late. The outer rims of the quartz crystals are outlined by abundant Type-2 fluid inclusions, which form sequential bands delineating the last incremental quartz growth stage. Because of their optical darkness, no analytical measurement was carried out on this type of fluid inclusion. Furthermore, fluid inclusions hosted within the intergranular fracture arrays are too small to be microthermometrically measured.

6.b. Footwall veins (F3 samples)

Well visible are dense arrays of fluid inclusions along healed microfracture trails, with mutual overprinting relationships (Fig. 7c). This microtextural arrangement did not always allow an accurate assessment of temporal relationships between trapped fluid inclusions. The presence of bigger (up to 25–30 μm) and more isolated and randomly distributed inclusions should indicate an earlier origin compared to the various trails. Early fluid inclusions are distinguished from late inclusions by shape and size (Fig. 7b). The former show irregular shape and dimension, whereas the latter are very uniform in shape (oval, rectangular, cubic) and their sizes reach 10–15 μm. The latest trapping event (intergranular trails) is evidenced by fluid inclusions too small to be microthermometrically measured. Both early and late fluid inclusions contain two phases, L + V (Type-2), with the liquid being dominant over the vapour with a constant V/V + L ratio (Fig. 7b). Nevertheless, scattered cases of V-rich inclusions have been observed. No sign of gas in the vapour phase was recorded. Finally, the presence of big (up to 40 μm), mostly decrepitated inclusions were also observed, and for them it might be suggested an earlier origin compared to the various trails (Fig. 7c).

6.c. Microthermometry

Conventional freezing and heating microthermometric analyses were carried out according to the procedure outlined in the Appendix. We measured inclusions occurring either in isolated clusters or within intragrain trails (Type-1 and -2 in FIL and F3 samples) and those defining the quartz growth zoning (Type-2 in FIL samples). In the FIL samples, Type-1 fluid inclusions

https://doi.org/10.1017/S001675681000097X Published online by Cambridge University Press

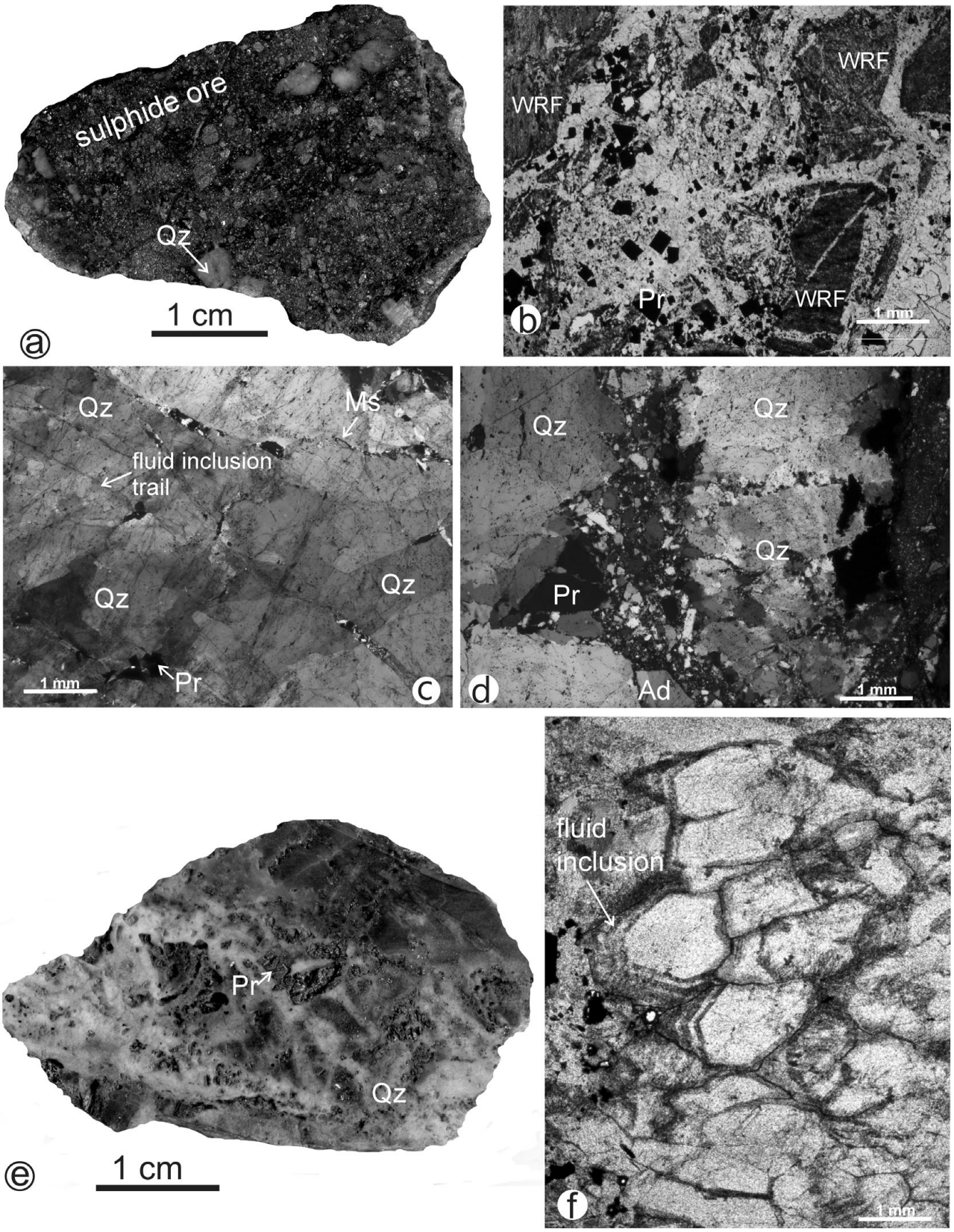

Figure 6. (a) Photograph of rock slab showing textures of veins and breccias in the footwall of the Boccheggiano Fault, with abundant pyrite mineralization hosted by quartz. (b) Microtexture at the thin-section scale (natural light) of the rock slab shown in (a), showing brecciated wall-rock fragments (WRF), healed by quartz–pyrite ore. (c) Quartz microtextures in sample (a) show multiple episodes of healed microfractures, marked by arrays of fluid inclusions (crossed polars). (d) Multiphase fracturing and brecciation at the thin-section scale for sample shown in (a), healed by quartz–adularia sulphide ore (crossed polars). (e) Photograph of rock slab showing sulphide ore mineralization in the Filone di Boccheggiano, hosted by quartz–adularia–sericite gangue. (f) Thin-section of the sample shown in (e) showing euhedral quartz grain with well-preserved growth structures marked by dense arrays of fluid inclusions. Ad – adularia; Ms – muscovite; Pr – pyrite; Qz – quartz; WRF – wall-rock fragments.

https://doi.org/10.1017/S001675681000097X Published online by Cambridge University Press

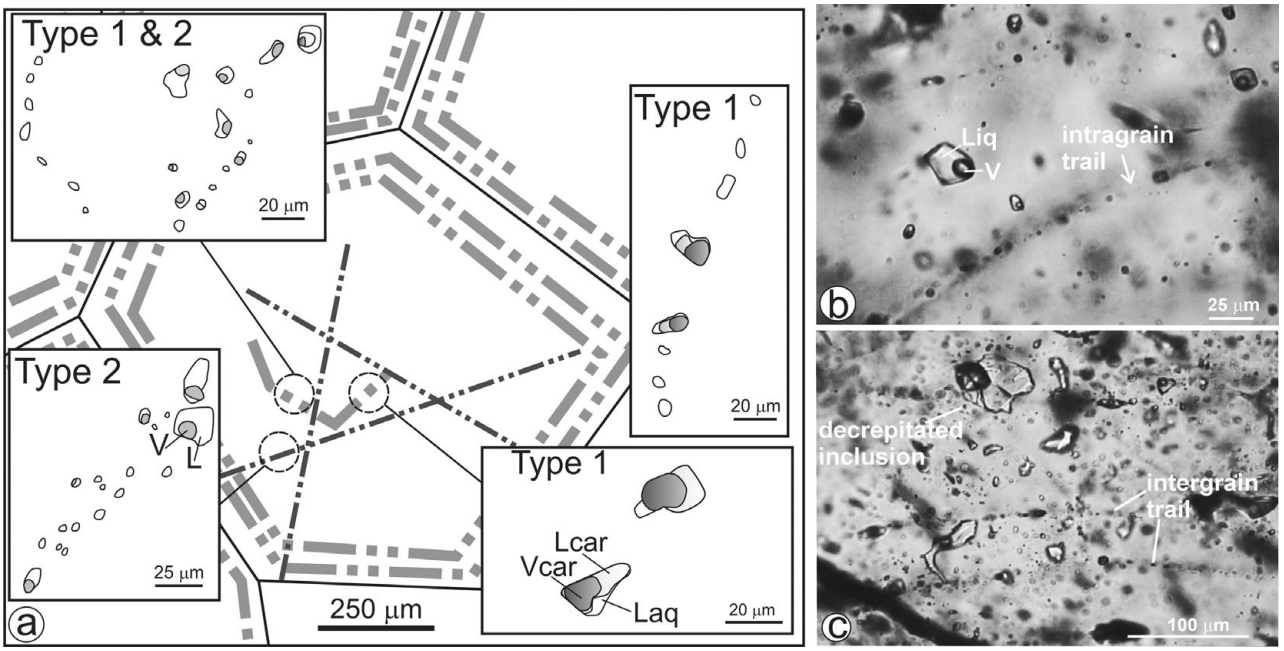

Figure 7. (a) Schematic line drawing of the fluid inclusion types and characteristics hosted in the quartz crystals associated with the ore mineralization in the Filone di Boccheggiano (FIL sample). (b) Primary and secondary Type-2 inclusions hosted in quartz from brecciated sulphide veins at the footwall of the Boccheggiano Fault (F3 sample). (c) Decrepitated fluid inclusions hosted in quartz from brecciated sulphide veins from F3 sample.

have a temperature of melting of the vapour phase T_m(V) at −56.6 °C, indicating the trapped gas is pure CO_2. Temperatures of homogenization of the carbonic phase ($T_{h\text{-}car}$) are very consistent and group at +31 °C, homogenizing in the majority of cases to the vapour phase (see Fig. A2 in the online Appendix at http://journals.cambridge.org/geo); in a few cases they show fading of the meniscus between L_{car} and V_{car}, probably towards the liquid carbonic phase. When detected, total homogenization for the three-phase fluid inclusions occurred to the vapour phase at temperatures ($T_{h\text{-}tot}$) ranging between 270 and 290 °C. Type-2 fluid inclusions from intragrain trails show T_h values from 220 to 310 °C, with a distinctive peak at 250–260 °C (see Fig. A2 in the online Appendix at http://journals.cambridge.org/geo). Apparent salinity values as converted from final melting temperature of ice ($T_{m\text{-}ice}$) span from 0 to 9 wt % NaCl equiv., with a gap between 3 and 6 wt % NaCl equiv. (Fig. 8). Apparent salinity data within the single trails are very consistent. It was not possible to measure any eutectic temperatures (T_e). Since Type-2 inclusions froze at about −36°C, we excluded the presence of cations other than Na and considered the fluid as a H_2O–NaCl system. In an inner quartz vein crystal from the FIL samples, occurrence in the same group of coexisting three-phase V-rich and two-phase L-rich inclusions was also observed. Microthermometric results indicate they homogenize to the vapour and the liquid at around 290 °C and 250 °C, respectively, indicating fluid immiscibility.

In the F3 samples, homogenization temperatures between liquid and vapour range from 250 to 360 °C, clustering at 280–290 °C. Rare cases of homogenization to the vapour phase have been

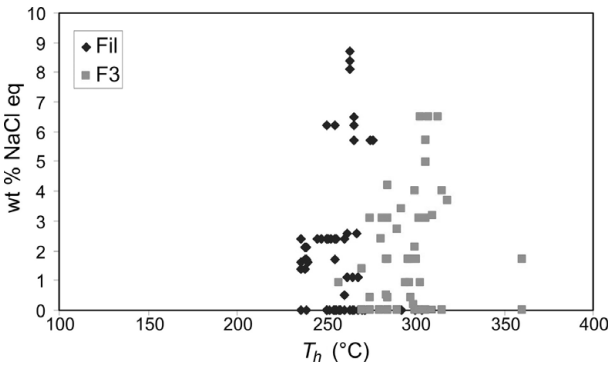

Figure 8. Homogenization temperature (T_h)–salinity diagram for quartz ore veins from both the fault hangingwall (FIL samples) and footwall (F3 samples).

measured at 360 °C (see Fig. A2 in the online Appendix at http://journals.cambridge.org/geo). No sign of gas in the vapour phase was detected. Salinity values range from 0 up to 7 wt % NaCl equiv. (Fig. 8). Only two T_e measurements were obtained at about −23 °C. Analogously to the FIL samples, since the inclusions froze between −35 and −40 °C, we excluded the presence of different cations besides Na. The occurrence of L-rich and V-rich inclusions in the same group has been observed in a few cases, homogenizing at about 290–300 °C to the liquid and to the vapour, respectively. This suggests that a boiling episode might have occurred.

Collectively, these data indicate that homogenization temperatures were about 30 °C higher for the fluid inclusions hosted in the F3 samples with respect to those hosted in the FIL ones. Microthermometric data are quite consistent, indicating the fluid(s) did

https://doi.org/10.1017/S001675681000097X Published online by Cambridge University Press

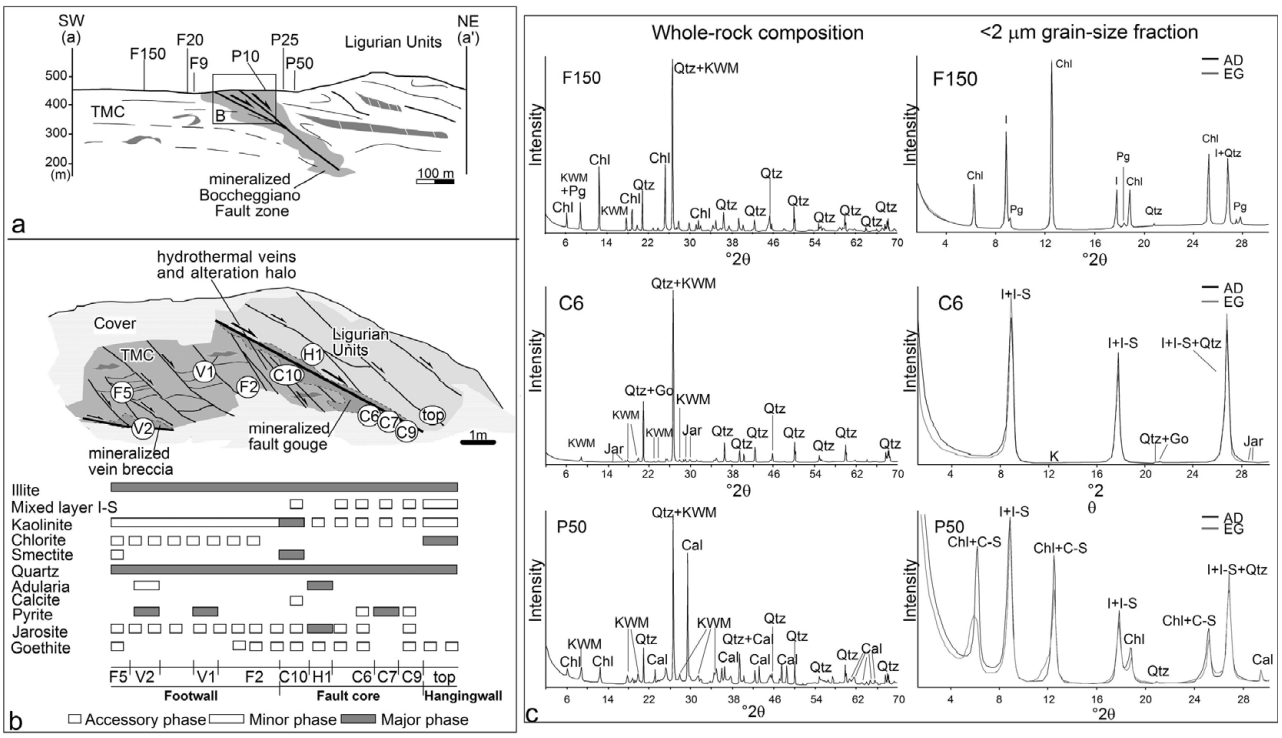

Figure 9. (a) Schematic geological cross-section across the BF with sample locations. (b) Enlargement of (a) showing the fault rock architecture across the fault core with related mineralogical assemblages. (c) Selected X-ray diffraction patterns of the whole-rock composition (to the right) and of the oriented, air dried (AD) and ethylene glycol-solvated (EG) mounts (to the left) of samples F150, C6 and P50. Cal – calcite; Chl – chlorite; C-S – chlorite-smectite mixed layers; Go – goethite; I – illite; I-S – illite-smectite mixed layers; Jar – jarosite; K – kaolinite; KWM – K-white mica; Pg – paragonite; Qtz – quartz.

not experience significant thermal change during the trapping events. On the other hand, the T_h versus salinity diagram (Fig. 8) shows an isothermal mixing/dilution trend between a low-medium salinity (9–7 wt % NaCl equiv.) fluid and an essentially salt-free meteoric water.

7. Wall rock alteration

7.a. Alteration mineralogy and zoning

A suite of 17 samples was collected along a 500 m long transect and analysed by XRD diffraction in order to evaluate modes and types of hydrothermal alteration across the BF, and to define the mineralogical assemblages associated with the texturally late sulphate mineralization episode. Four samples are from the hangingwall rocks (Ligurian units) and the fault gouge, five from the footwall rocks (Tuscan Metamorphic Complex). Three additional samples were collected from veins parallel to the main foliation in the footwall and one from the late-stage sulphate mineralization (Fig. 9a, b). XRD qualitative and quantitative analysis of the whole-rock mineralogy and the <2 μm grain-size fraction is shown in Tables 1 and 2, respectively. Hydrothermal alteration types are described here using the nomenclature based on the dominant mineral (or group of minerals) that characterizes each assemblage (e.g. Reyes, 1990).

In the footwall rocks, an unaltered sample (F150; Fig. 9c) is characterized by quartz, K-white mica, chlorite and subordinate paragonite. Minor amounts of albite and graphite locally observed in the Tuscan Metamorphic Complex by Costantini *et al.* (2002) were not identified. Among major minerals, chlorite abruptly decreases in concentration and K-white mica alters in a series of fine-grained and interstratified minerals moving towards the fault zone. Retrograde alteration of high-temperature micas is accompanied by a loss in sharpness of the 001 peak and progressive formation of small illite particles and low expandable mixed-layer illite-smectite (sample C6; Fig. 9c). In the <2 μm grain-size fraction, illite is ubiquitous and kaolinite increases in abundance towards the fault plane reaching the maximum concentration at the contact with the mineralized fault gouge (sample C10; Fig. 9b; Table 2). Alteration selvages around quartz + pyrite veins consist of quartz, K-feldspar (adularia), illite, jarosite, goethite and kaolinite, a mineral assemblage that suggests multiple episodes of mineral deposition and chemical weathering. The fault gouge samples (C6, C7, C9, C10) mainly consist of quartz, K-white mica and pyrite. Calcite, jarosite and goethite are present as minor phases. In their <2 μm fractions, illite is the most abundant clay mineral; smectite and kaolinite are found in minor quantities and mixed-layer illite-smectite occurs only in small amounts (<2 %). Chlorite is absent. This alteration assemblage is compatible with the argillic alteration type.

In the hangingwall rocks, an unaltered sample (P50; Fig. 9c) from the Ligurian unit is mainly composed of quartz, calcite, K-white mica and clay minerals such as chlorite and mixed-layers illite-smectite and

https://doi.org/10.1017/S001675681000097X Published online by Cambridge University Press

Table 1. Mineralogy of the whole-rock samples

			Mineralogy of the whole rock											
Sample	Unit	Rock type	Qtz	Cal	Kfs	KWM	Pg	K	Chl	I-S	C-S	Sm	Jar	Pr	Go
F150	TMC	phyllites	**			**	*		**						
F20	TMC	phyllites	**			**	*	*	**	*			*		
F9	TMC	phyllites	**			**		*		*			*		
F5	TMC	phyllites	**			**		*	*			*	*		*
F2	TMC	phyllites	**			**		*	*				*		*
C10	Fault gouge	breccia	**	*		**		*				*	*		*
C6	Fault gouge	breccia	**			**		*		*			*	*	*
C7	Fault gouge	breccia	**			**		*		*				**	
C9	Fault gouge	breccia	**			**		*		*			*	*	*
top	Ligurian Unit	pelite	**			*		*	*	**					*
P10	Ligurian Unit	pelite	**		**	*			*						
P25	Ligurian Unit	pelite	**		*	*			**	*					
P50	Ligurian Unit	marl	**	**		**			**	*	*				
V1	Vein	–	**			*		*	*	*			*	**	
V2	Vein	–	**		*	*		*	*				*	**	
H1	Alteration halo	–	**		**	*		*					**		*

Abbreviations: Qtz – quartz; Cal – calcite; Kfs – K-feldspar; KWM – K-white mica; Pg – paragonite; K – kaolinite; Chl – chlorite; I-S – illite–smectite mixed layers; C-S – chlorite–smectite mixed layers; Sm – smectite; Jar – jarosite; Pr – pyrite; Go – goethite. ** – major phase; * – minor phase.

Table 2. X-ray quantitative analysis of the <2 μm grain-size fraction

		X-ray quantitative analysis of the <2 μm grain-size fraction (wt %)										
Sample	Unit	Sm	I	Pg	I-S	C-S	K	Chl	Other	R	% I in I-S	% C in C-S
F150	TMC	–	42	4	–	–	–	54	Qtz	–	–	–
F20	TMC	–	42	2	1	–	10	45	Qtz, Jar	3	99	–
F9	TMC	–	83	–	1	–	16	–	Qtz, Jar	3	99	–
F5	TMC	7	75	–	tr	–	16	2	Qtz, Jar	–	–	–
F2	TMC	–	78	–	tr	–	20	2	Qtz, Jar, Go	–	–	–
C10	Fault gouge	16	37	–	tr	–	47	–	Qtz, Jar, Go	–	–	–
C6	Fault gouge	–	99	–	1	–	tr	–	Qtz, Jar, Go	3	93	–
C7	Fault gouge	–	99	–	1	–	tr	–	Qtz, Pr	3	94	–
C9	Fault gouge	–	97	–	2	–	1	–	Qtz, Go	3	94	–
top	Ligurian Unit	–	20	–	58	–	6	16	Qtz, Go	3	91	–
P10	Ligurian Unit	–	41	–	–	–	–	59	Qtz	–	–	–
P25	Ligurian Unit	–	40	–	7	–	–	53	Qtz	3	90	–
P50	Ligurian Unit	–	52	–	6	18	–	24	Qtz, Cal	3	90	75
V1	Vein	–	92	–	1	–	5	3	Qtz, Jar	3	94	–
V2	Vein	–	tr	–	–	–	16	84	Jar	–	–	–
H1	Alteration halo	–	94	–	–	–	6	–	Jar	–	–	–

Abbreviations: Sm – smectite; I – illite; Pg – paragonite; I-S – illite–smectite mixed layers; C-S – chlorite–smectite mixed layers; K – kaolinite; Chl – chlorite; R – stacking order (Jagodzinski, 1949); % I in I-S – illite content in illite–smectite mixed layers; % C in C-S – chlorite content in chlorite–smectite mixed layers; tr – trace; Qtz – quartz; Jar – jarosite; Go – goethite; Pr – pyrite; Cal – calcite.

chlorite-smectite. Moving towards the fault zone, calcite disappears and K-feldspar (adularia) crystallizes (samples P25 and P10). Goethite was observed in the most altered sample. In the <2 μm grain-size fractions, illite progressively decreases in abundance from 52 to 20 % and mixed-layer illite-smectite increases from 6 to 58 %. This trend is diagnostic of the illite alteration type.

Samples of the late mineralization document the occurrence of different kinds of hydrated Fe-sulphates (paracoquimbite, coquimbite) and Fe-sulphate hydroxides (ferricopiapite, copiapite) associated with quartz.

7.b. Whole-rock geochemistry and mass balance

The nature and extent of the alteration processes in the fault zone rocks were quantified by comparing the whole-rock chemistry of the damage zone rocks to that of their undeformed protoliths, based on a suite of samples collected along the profile shown in Figure 9a. The protoliths were defined by the average composition of three samples arbitrarily distributed over several hundreds of metres at the fault footwall (TMC; sample F150 in Fig. 9; Table 3) and hangingwall (Ligurian Complex; sample P50 in Fig. 9; Table 3). Standard deviations for most major elements are typically below 1 %, indicating little compositional variation within the selected lithologies. In order to reduce the influence of unhomogeneities caused by ore bodies within the damage zone of the BF, samples were collected carefully excluding quartz and sulphide veins.

Element gains and losses were calculated by the mass balance isocon method of Grant (1986). Plotting C^0 versus C^A of immobile elements defines a line that passes through the origin (the isocon line), whose equation is as follows:

$$C^A = (M^0/M^A)C^0 \quad (2)$$

where C^0 and C^A are the element concentrations in the unaltered and altered rocks, respectively, M^A is the mass

https://doi.org/10.1017/S001675681000097X Published online by Cambridge University Press

Table 3. Representative whole-rock data of altered and unaltered samples of footwall and hangingwall rocks from the damage zone of the Boccheggiano Fault

		Footwall (TMC, Boccheggiano Fm)						Hangingwall (Ligurian Complex)								
		Protolith (av. #3)		Alteration (av. #4)		ΔC_i	$\Delta C_i/C_0$ (%)	Protolith (av. #3)		Alteration (av. #3)		ΔC_i	$\Delta C_i/C_0$ (%)	Filone	ΔC_i	$\Delta C_i/C_0$ (%)
density (g cm^{-3})		2.82		2.71				2.78		2.66				2.89		
			1σ		1σ				1σ		1σ					
SiO_2	(%)	53.64	1.63	70.09	3.06	49.44	92	49.52	1.15	84.37	3.06	65.12	131	85.33	135.97	275
Al_2O_3	(%)	24.44	0.96	12.80	1.31	−5.62	−23	18.91	0.82	6.89	1.31	−9.56	−51	1.09	−16.54	−87
MnO	(%)	0.04	0.01	0.00	0.00	−0.03	−85	0.08	0.01	0.04	0.00	−0.03	−34	0.01	−0.07	−84
MgO	(%)	2.55	0.14	0.51	0.07	−1.80	−70	3.69	0.38	0.24	0.07	−3.37	−91	0.28	−3.09	−84
CaO	(%)	0.09	0.01	0.00	0.00	−0.09	−100	3.79	1.03	0.07	0.00	−3.70	−98	0.10	−3.58	−95
Na_2O	(%)	1.08	0.09	0.09	0.03	−0.95	−88	0.71	0.02	0.00	0.03	−0.71	−100	0.01	−0.69	−97
K_2O	(%)	4.21	0.26	4.30	0.67	2.12	50	2.81	0.03	1.64	0.67	−0.59	−21	0.22	−2.34	−83
TiO_2	(%)	1.08	0.03	0.72	0.02	−0.03	−3	0.77	0.01	0.57	0.02	0.00	0	0.04	−0.68	−89
P_2O_5	(%)	0.10	0.00	0.05	0.04	−0.03	−29	0.08	0.00	0.01	0.04	−0.06	−80	0.01	−0.07	−86
Fe_2O_3(Tot)	(%)	8.22	0.03	7.82	2.19	3.28	40	12.30	1.56	1.51	2.19	−10.25	−83	8.30	5.74	47
LOI	(%)	6.11	0.43	3.56	0.36	−0.87	−14	10.12	0.45	3.261	0.36	−5.69	−56	3.89	−1.66	−16
Total	(%)	101.56		99.95				102.78		98.59				99.25		
V	(ppm)	117.7	28.7	89.8	10.8	14.3	12	118.2	3.4	71.5	44.9	−21.0	−18	1.9	−114.0	−96
Cr	(ppm)	86.9	24.8	59.6	5.0	0.7	1	91.9	3.1	36.0	17.8	−42.9	−47	1.0	−89.8	−98
Co	(ppm)	26.2	12.1	30.5	10.8	18.6	71	21.6	2.5	59.6	29.8	59.4	275	402.8	854.1	3952
Ni	(ppm)	15.3	3.6	0.0	0.0	−15.3	−100	47.3	3.5	0.0	0.0	−47.3	−100	0.0	−47.3	−100
Cu	(ppm)	0.0	0.0	12.3	13.5	18.0	–	0.0	0.0	0.0	0.0	0.0	–	0.0	0.0	–
Zn	(ppm)	104.5	50.7	32.2	29.6	−57.2	−55	108.1	4.1	11.1	5.1	−93.1	−86	9.3	−87.9	−81
Ga	(ppm)	22.8	6.9	17.8	0.4	3.5	15	20.1	0.9	12.7	4.4	−2.8	−14	0.7	−18.5	−92
Ge	(ppm)	0.8	0.3	0.5	0.4	0.0	–	0.2	0.0	0.6	0.6	0.6	245	4.2	8.8	3842
As	(ppm)	18.5	4.8	87.1	54.4	109.6	593	4.5	0.2	15.8	3.3	16.9	374	127.7	273.2	6038
Rb	(ppm)	152.5	41.2	205.0	30.8	149.0	98	116.7	0.7	114.0	80.1	38.1	33	2.8	−110.6	−95
Sr	(ppm)	100.2	34.9	48.0	10.1	−29.5	−29	153.7	18.1	99.6	46.9	−18.4	−12	3.7	−145.6	−95
Y	(ppm)	28.8	10.4	10.1	2.2	−14.0	−48	22.4	1.1	16.9	4.2	0.6	3	1.1	−20.1	−90
Zr	(ppm)	173.1	21.7	162.9	34.8	66.4	38	112.1	1.7	98.9	53.3	22.3	20	0.0	−112.1	−100
Nb	(ppm)	17.6	5.0	14.7	1.1	4.0	23	16.4	0.7	8.5	5.1	−4.9	−30	3.8	−8.2	−50
Ag	(ppm)	0.1	0.1	1.4	1.3	2.0	1879	0.5	0.5	2.7	2.7	3.1	619	3.1	6.3	1234
Cd	(ppm)	1.0	0.6	2.0	0.6	1.8	179	1.1	1.1	0.8	0.4	0.0	−1	3.6	6.6	580
La	(ppm)	42.9	14.0	4.3	0.9	−36.6	−85	33.8	3.3	14.7	1.7	−13.8	−41	0.0	−33.8	−100
Ce	(ppm)	84.9	28.9	8.7	6.7	−72.2	−85	65.2	2.0	30.6	13.9	−23.7	−36	4.1	−56.3	−86
Pr	(ppm)	7.9	2.9	1.4	1.8	−5.9	−75	2.6	0.2	4.2	2.2	3.1	118	0.1	−2.4	−92
Nd	(ppm)	38.8	14.1	6.0	0.9	−29.9	−77	30.5	1.0	14.0	5.1	−11.5	−38	5.4	−18.8	−62
Sm	(ppm)	5.7	3.1	0.8	1.4	−4.6	−80	7.8	2.1	3.7	0.9	−2.8	−36	3.5	−0.1	−2
Yb	(ppm)	3.7	0.6	2.1	0.3	−0.6	−15	1.1	1.1	3.1	0.1	3.1	277	10.9	22.6	2040
Th	(ppm)	11.9	4.6	5.1	1.0	−4.4	−37	8.4	0.2	0.6	0.6	−7.5	−90	0.0	−8.4	−100
U	(ppm)	0.5	0.6	0.0	0.0	−0.5	−100	0.3	0.3	0.1	0.1	−0.1	−45	0.0	−0.3	−100

of the altered rock and M^0 is the mass of the protolith. The slope of the isocon (M^0/M^A) is obtained from a best-fit of the analytical data forming a linear array through the origin; the variation in the absolute concentrations of the elements (ΔC_i) from the unaltered to the altered rocks is given by the equation:

$$\Delta C_i = (M^A/M^0)C^A - C^0 \qquad (3)$$

Calculations were obtained though the software GEOISO (Coelho, 2005). The results of the major element mass balance calculations are different when moving from the footwall to the hangingwall rocks of the BF (Fig. 10). In the TMC footwall rocks, mass balance was carried out by comparing the protolith composition with an average composition obtained from four samples collected within the alteration zone from 5 to 10 m from the fault core (sample F2 in Fig. 9 and Table 3). The isocon line was calculated using Ti, Cr and Ge as immobile elements, which gives $M^0/M^A = 0.68$, corresponding to a ~47 % mass gain and a ~53 % volume increase (Fig. 10a). For the major elements, this was achieved by removal of Ca, by the almost total removal of Mg (decrease of 70 %), Mn (decrease of 85 %), Na (decrease of 88 %), and by reduction of P (decrease of 29 %), Al (decrease of 23 %) and LOI. These depletions are in part counterbalanced by the increase of Si (increase of 92 %), K (increase of 50 %) and Fe (increase of 40 %). Among the trace elements, Rb and Ba show significant gains, which correlates well with the high K_2O content and illitization of the alteration zone. For the base and precious metals, Cu and Ag concentrations show significant increases (enrichment by >18 times); As is also enriched (~6 times), while Ni and Zn show depletions.

In the Ligurian hangingwall rocks, the wall rock alteration was calculated by comparing the protolith composition with the composition of samples obtained from the alteration zone at different distances from the fault core: (i) an average composition obtained from three samples collected at *c*. 10 m from the fault core (sample P10 in Fig. 9; Table 3), where the major alteration is observed, and (ii) a composition obtained from samples of the Filone di Boccheggiano, in the immediate fault hangingwall (sample H1 in Fig. 9; Table 3). For sample P10, the isocon line was constructed using Ti, Cd and Y as immobile elements, which gives $M^0/M^A = 0.74$, corresponding to a ~36 % mass gain and a ~42 % volume increase (Fig. 10b). Intense silicification is documented by the sole gain of SiO_2 (increase of 132 %) and the total depletion of the other major elements, with the removal of Na_2O and the almost total removal of CaO and MgO (decrease of 98 and 91 %, respectively). Depletions in Fe_2O_3, P_2O_5, LOI and Al_2O_3 are significant (decrease of 83, 81, 56, and 51 %, respectively); depletion in K_2O is minor (decrease of 21 %). Also in this case, alteration is associated with an enrichment in Ag (>6 times) and As (>3 times). No Cu enrichment is reported, while the Rb and Ba gains are compatible with adularia crystallization.

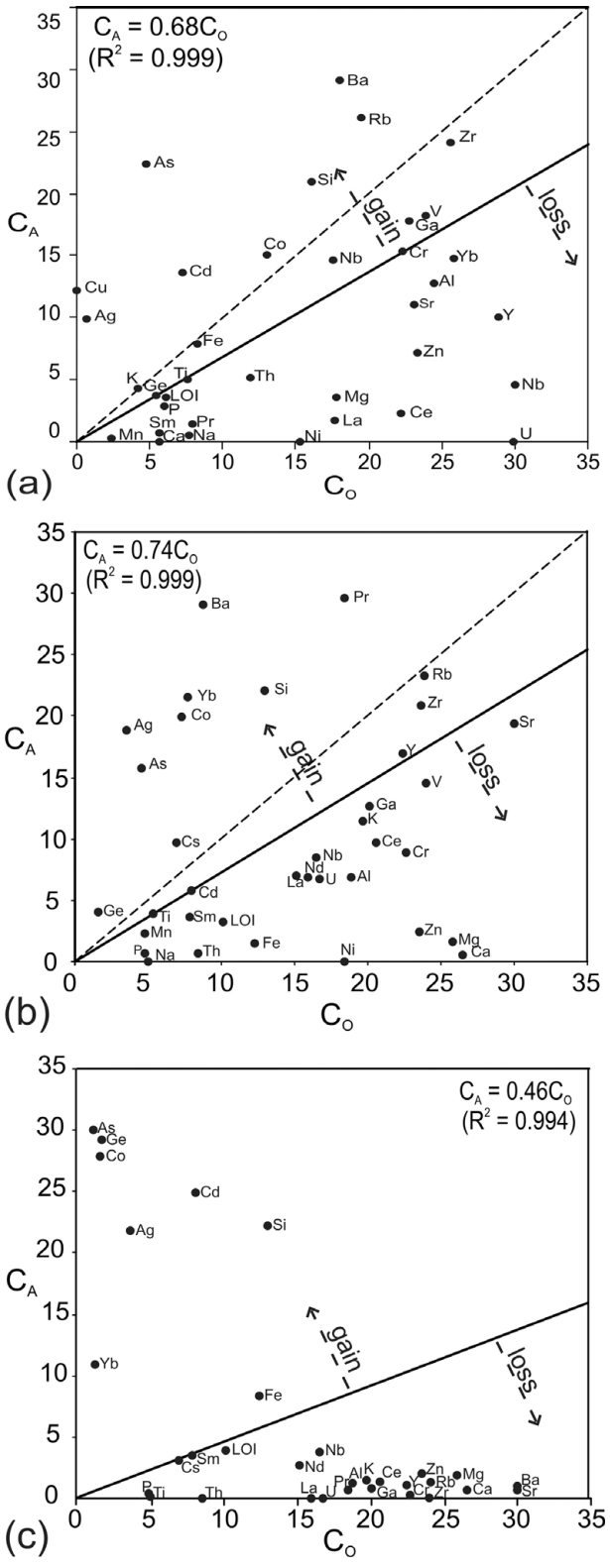

Figure 10. Element abundance within different portions of the damage zone of the BF versus original wall rock abundances, scaled by random factors. (a) Footwall of the fault; (b) and (c) hangingwall of the fault. Major element abundances are in wt % oxides; trace elements are in ppm. Dashed line is the constant mass reference frame. C^0 – unaltered composition; C^A – altered composition. Data from the profile shown in Figure 9 and reported in Table 3.

https://doi.org/10.1017/S001675681000097X Published online by Cambridge University Press

For sample H1, whole-rock analytical data show the systematic decrease of most of the element concentrations (also those commonly assumed to be immobile, such as Al, Ti, Zr and Y) and an abrupt increase in Si (Fig. 10c). The isocon line was calculated using Cs and Sm as immobile elements, which gives $M^0/M^A = 0.46$, corresponding to a ~119 % mass gain and a ~109 % volume increase. Notable among the major elements is the enrichment of SiO_2 by >2 times and the gain in Fe_2O_3 (increase of 47 %), compensated by the almost total removal of Al, Na, Ca, Mg, Mn and K. Particularly significant is the enrichment of metals such as As (>60 times), Cd, Yb and Ag (>12 times).

8. Stable isotope analyses

Oxygen isotope analysis was performed on quartz samples collected from sulphide veins both in the footwall and in the hangingwall of the BF. The isotopic compositions of the quartz veins range from 8.31 ‰ to 10.15 ‰ (footwall) and 8.05 ‰ to 9.67 ‰ (hangingwall), respectively. For the full results see Table A1 in the online Appendix at http://journals.cambridge.org/geo. The average values of the two types of quartz (9.0 ‰ and 9.1 ‰ for the footwall and the hangingwall, respectively) indicate that both deposits equilibrated isotopically with the same oxygen reservoir. The temperature of equilibration of about 300 °C, measured from fluid inclusion microthermometric determinations (this study and Liotta *et al*. 2009), allows us to calculate the isotopic composition of the water phase of the fluid where quartz precipitated. This estimation requires crucial assumption of isotopic equilibrium and the choice of one of the many experimental and theoretical expressions relating the isotopic compositions of water, quartz and temperature. Using the equation of Clayton, O'Neil & Mayeda (1972) recalculated by Friedman & O'Neil (1977), it was inferred that the formation of quartz occurred within a fluid whose aqueous phase isotope composition was bracketed between 0.55 and 2.39 ‰ and 0.29 and 1.91 ‰ for the footwall and the hangingwall veins, respectively. Also taking into consideration the data reported in Liotta *et al*. (2009), the isotopic water composition can be interpreted in terms of mixing of meteoric water and the aqueous component of fluids of magmatic provenance and/or isotopically equilibrated with the host rocks. It is furthermore evident that quartz–sulphide segregation and genesis of the Filone di Boccheggiano derived from the same fluid system, under similar thermal conditions.

9. Discussion

Fault rocks across the BF were infiltrated by fluids that changed their structural fabric, mineralogy and major element geochemistry. The presence of an active fluid phase within the damage zone of the BF is indicated by (i) veining and mineralized breccias in the phyllonite gouge, and (ii) precipitation of an interconnected network of phyllosilicate aggregates in cataclasites, which suggests that fluid-assisted diffusive mass transfer operated during formation of the phyllonite gouge (see also Jefferies *et al*. 2006). Geochemical alteration features across the fault document that fluid circulation was systematically associated with the removal of Ca, Mg, Na and Al from the protoliths, largely compensated by Si (and partly K) enrichment that is maximum in the immediate hangingwall of the fault. This general pattern of rock alteration and element mobility is predicted to occur during down-temperature fluid flow (Dipple & Ferry, 1992), a flow regime commonly predicted for active hydrothermal systems (e.g. Henley, 1985).

Collectively, the ore-associated dominant argillitic alteration mineralogy and zoning within the damage zone of the BF, as well as the textures dominated by multiple episodes of mineral deposition and fracturing show characteristics typical of the low-sulphidation (near-neutral pH) epithermal environments (e.g. Giggenbach, 1992; White & Hedenquist, 1995; Einaudi, Hedenquist & Inan, 2003; Simmons, White & John, 2005). This is in accordance with (i) the presence of adularia and illite associated with quartz as the main gangue minerals in the ore deposits and (ii) the isotopic signature and the trend in fluid mixing evidenced by the fluid inclusions (see also Liotta *et al*. 2009), both documenting a fluid dominated by a meteoric supply. Approaching the core of the BF (in both the footwall and hangingwall rocks) and in alteration selvages surrounding the quartz ore veins in the footwall, an incipient advanced style of argillitic alteration is also present, as indicated by kaolinite associated with jarosite. The increase of kaolinite abundance towards the fault core suggests a high degree of fluid–rock interaction, attesting that the major palaeofluid conduits were created in the rock volume adjacent to the fault core. The presence of smectite in the fault core (Fig. 9b) reflects changes in chemical and fluid–rock conditions, since its crystallization together with kaolinite strongly depends on pH or Na^+/H^+ or Ca^{2+}/H^+ variations (Velde, 1985). It is thus deduced that the high-permeability conduits within the damage zone of the BF also constituted preferred pathways for degassing of the hydrothermal system, with formation of steam-heated acid-sulphate waters from oxidation of H_2S (cf. Giggenbach, 1992). This argues for late-stage acid-sulphate alteration of the low-sulphidation system during post-hydrothermal weathering of the sulphide minerals, typical of the epithermal discharge of steam-heated acid waters convecting into the upper part of a hydrothermal system (e.g. Henley, 1985; White & Hedenquist, 1995).

9.a. *P–T* conditions of fluid entrapment

The microthermometric results may contribute to elucidating the physico-chemical process associated with sulphide ore formation during hydrothermal outflow along the damage zone of the BF. The presence of coeval CO_2-rich fluid inclusions and

https://doi.org/10.1017/S001675681000097X Published online by Cambridge University Press

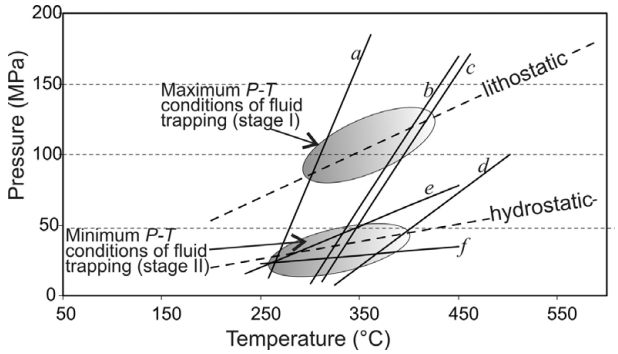

Figure 11. Pressure–temperature diagram with isochores for the different types of fluid inclusions: Type-1 CO_2-bearing and aqueous Type-2 fluid inclusions hosted in quartz veins from the Boccheggiano ore deposit. Crossing of isochores of the two coeval immiscible fluids defines their trapping conditions. Also shown are lithostatic and hydrostatic thermobaric gradients based on a palaeogeothermal gradient of 90 °C km^{-1} (see text for further details).

L-rich aqueous inclusions in the mineralizing fluids responsible for formation of the Filone di Boccheggiano ore (FIL samples) documents a fluid immiscibility at the time of the inclusion formation that occurred during the rising of the fluids along the conduits (Hedenquist & Lowerstern, 1994; Bodnar, 1995 and references therein). It is known that in this case, homogenization temperatures can be considered as the trapping temperature (Roedder, 1984), and isochores of immiscible saline fluids and CO_2-rich inclusions provide constraints on the fluid pressure–temperature (*P–T*) trapping conditions during quartz vein formation (cf. Bodnar, 1995). In F3 samples, the occurrence, even though sporadic, of L-rich and V-rich Type-2 inclusions in the same group, homogenizing at about the same temperature (290–300 °C) to the liquid and to the vapour phase respectively, suggests that episodic boiling conditions occurred during the footwall vein formation. Homogenization temperatures can be considered as well as trapping temperatures (Roedder, 1984).

Fluid inclusion isochores (Fig. 11) have been constructed using the program package FLUIDS by Bakker (2003). Isochores were chosen considering two representative fluid inclusions for each type and sample: (i) two for the aqueous Type-2 inclusions of the FIL samples, labelled *a* and *c*; (ii) two for the Type-1 carbonic inclusions of the FIL samples, labelled *e* and *f*; and (iii) two for the aqueous Type-2 inclusions of the F3 samples, labelled as *b* and *d*. Calculations were based on the equations of state of Sterner and Bodnar (1991) for isochores *a*, *e* and *f*; Haar, Gallagher, & Kell (1984) for isochores *b* and *d*; and Knight & Bodnar (1989) and Bodnar & Vityk (1994) for isochore *c*. Density values range from 0.80 (isochore *a*) to 0.20 (isochore *f*) g cm^{-3}. We then assumed a palaeogeothermal gradient of 90 °C km^{-1}, as reconstructed from the in-depth mineralogical zonation in the basement rocks of the Montieri area hosting the southern branch of the Larderello geothermal field (Rossetti *et al*. 2008). Lithostatic and hydrostatic thermobaric gradients are based on 27 MPa km^{-1} and 10 MPa km^{-1}, respectively. The *P–T* field defined by intersections of isochores is consistent with the hydrostatic thermobaric gradient of 90 °C km^{-1}. Accordingly, the minimum trapping pressure for fluid inclusions ranges between 30 and 50 MPa for temperatures in the order of 300–350 °C (stage II in Fig. 11). Intersections of the isochores *a*, *b* and *c* with the lithostatic gradient line define maximum trapping conditions of 80–130 MPa (stage I in Fig. 11) and argue for nearly isothermal transient and fluctuating fluid pressure conditions (from (supra)lithostatic to hydrostatic) within the damage zone of the BF during sulphide ore mineralization. Textures in the wall rocks provide evidence for fracturing and subsequent crack-sealing by precipitation of quartz–adularia–sulphide assemblages. In addition, evidence for pressure changes during fluid infiltration along the BF can be also deduced by the decrepitation textures in some of the fluid inclusion assemblages (Fig. 7c; see Oliver *et al*. 2006) and is consistent with boiling of the hydrothermal fluids.

9.b. Fluid fluxes and the hydraulic transmissivity model

As most of the protolith rocks cut across by the BF are quartz-bearing, the Si content in the fault rocks is likely to reflect changes in solubility due to the decreasing temperatures of the infiltrating fluids. The amount of quartz precipitated/dissolved in an advective flow regime can be then used to constrain the volume of metasomatizing fluids, assuming local fluid–rock equilibrium and ignoring dispersion (e.g. Streit & Cox, 1998; Cartwright & Buick, 1999). In these calculations it is also assumed that silica solubility in the circulating fluids is approximately that of SiO_2 in pure water and that silica precipitation was controlled only by changes in *P–T* (e.g. Fournier & Potter, 1982). This is justified by the fluid inclusion results, documenting the presence of two-phase, low salinity, H_2O-dominated fluid inclusions in mineralized quartz veins from the damage zone of the BF.

Understanding these assumptions, fluid fluxes, q (in mol m^{-2}), can be calculated via the equation (Dipple & Ferry, 1992):

$$q = \frac{n_i}{(\partial Xi/\partial T)_P(\mathrm{d}T/\mathrm{d}z) + (\partial Xi/\partial P)_T(\mathrm{d}P/\mathrm{d}z)} \quad (4)$$

where n_i is the change in concentration of the element i during alteration, $(\partial Xi/\partial T)_P$ and $(\partial Xi/\partial P)_T$ are the temperature and pressure dependencies, respectively, of the solubility of species i, and $\mathrm{d}T/\mathrm{d}z$ and $\mathrm{d}P/\mathrm{d}z$ are the temperature and pressure gradients along the fluid flow path, respectively. Being that the pressure dependency of quartz solubility is less significant than its temperature dependency, the second term of the denominator of equation (4) is commonly discounted when calculating fluid fluxes (e.g. Dipple & Ferry, 1992; Cartwright & Buick, 1999).

https://doi.org/10.1017/S001675681000097X Published online by Cambridge University Press

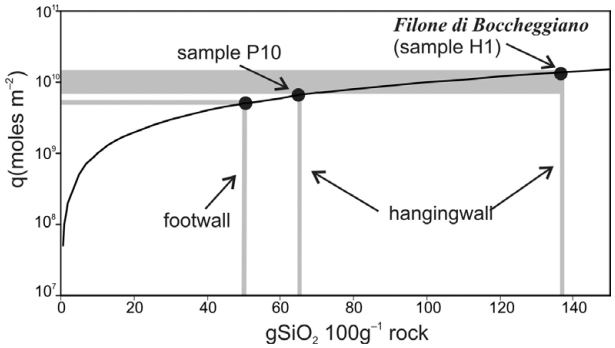

Figure 12. Curve showing the time integrated fluid flux q versus mass of quartz precipitated per 100 g of protolith (temperature of *c*. 300 °C; rock density from Table 3) for the damage zone of the Boccheggiano Fault. The shaded areas represent the ranges of Si mobility for both footwall and hangingwall alteration (see text for further details).

In the damage zone of the BF, increase of SiO_2 is distinctly different when moving from the footwall to the hangingwall rocks (Table 3), with values ranging from 40 to 140 g per 100 g, or, based on the rock density values shown in Table 3, from 1.8×10^4 to 6.2×10^5 mol Si m^{-3}. For the calculation we employed a temperature of 300–350 °C, as deduced from the fluid inclusion data presented in this study and the available thermometric data for the ore stage (Martarelli, Ferrini & Masi, 1995), and an average background temperature gradient during alteration of 90 °C km^{-1} (0.09 °C m^{-1}). The temperature derivative of the quartz solubility at 300 °C is in the order of 5×10^{-5} (Rimstidt, 1997). Given these parameters, time integrated fluid fluxes in the damage zone of the BF range between *c*. 4×10^9 and 1×10^{10} mol m^{-2}, when moving from the footwall to the hangingwall rocks, respectively (Fig. 12).

These data indicate that fluid flow in the damage zone of the BF was highly concentrated in the immediate hangingwall of the fault, with flow magnitudes higher for the hangingwall than for the footwall rocks. This is in agreement with the analysis of the fracture pattern in the fault rocks across the BF, documenting an abrupt decrease in the fracture abundance, and hence in the hydraulic transmissivity, moving from the hangingwall to the footwall rocks. This is also in agreement with the alteration mineralogy found respectively at the footwall and hangingwall of the fault. In particular, adularia is distributed in the hangingwall rocks and as a gangue mineral in the Filone di Boccheggiano at the immediate hangingwall of the BF, whereas it only seldom occurs in alteration halos surrounding mineralized veins at the footwall of the BF. Since the occurrence of adularia has been commonly used as an indicator of an intense water/rock ratio and correlated with the development of secondary porosity in hydrothermally altered rock sections (e.g. Moore *et al*. 2001), the pattern of adularia occurrence in the damage zone of the BF once again confirms that the hangingwall rocks have been by far subjected to the largest amount of fluid flow. Based on the above points, we propose that the fine-grained phyllonite fault gouge separated a low flow region below (footwall rocks) from a high flow one above (hangingwall rocks) and, hence, the fault gouge operated as a permeability barrier to fluid circulation, preventing fluid flow across the fault (see e.g. Caine, Evans & Forster, 1996; Sibson, 2000; Rowland & Sibson, 2004). This resulted in a highly anisotropic hydraulic transmissivity along the BF, with fluid flow being focused within the highly fractured damage zone at the fault hangingwall.

9.c. Model of fluid flow and mineralization

Collectively, the geological, fluid inclusion and geochemical information described above indicate that sulphide mineralization of the Campiano mine was primarily controlled by near-neutral pH thermal waters, circulating within permeable zones created within the damage zone of the BF. The main features involved during sulphide ore genesis along the BF may be summarized as follows: (i) highly anisotropic hydraulic transmissivity across the BF, with upward fault-parallel fluid flow occurring dominantly at the fault hangingwall; (ii) transient and fluctuating fluid pressure conditions during ore mineralization; (iii) a source of thermal energy (magmatic body) to account for the T_h values of the footwall vein fluids and the volume of fluid/vapour required to account for both the hydrothermal alteration and sulphide mineralization (the Late Pliocene Montieri pluton of Villa *et al*. (2006); (iv) deep circulation of meteoric water and mixing with magmatic fluid(s) to account both for the widespread variation in the $\delta^{34}S$ values in sulphides (Martarelli, Ferrini & Masi, 1995) and the range in fluid salinities that is a typical feature of epithermal ore environments worldwide (e.g. Heinrich, 2005).

Considering the above issues, we propose a model of fault-controlled hydrothermal fluid discharge along the BF during transition from a magmatic to hydrothermal environment at the southern branch of the Larderello geothermal field. This model is framed within the regional regime of extensional tectonics that accompanied the Neogene–Quaternary evolution of southern Tuscany. Meteoric fluids permeating along the steeply dipping fracture network created by extensional tectonics (Cameli, Dini & Liotta, 1993; Liotta *et al*. 2009) were firstly equilibrated at depth with their host rocks (rock-buffered circulation system), were reduced, and then they retained a near-neutral pH (Giggenbach, 1992). Convective fluid circulation at depth maintained by the cooling Montieri pluton was channelized along the anisotropic permeability structure of the BF that indeed constituted a major hydrothermal discharge conduit. The anisotropic structure of the fault damage zone across the fault core controlled the mode of fluid flow and mineralization. Fluid flow was structurally controlled and compartmentalized by the barrier of permeability constituted by the fault core that acted as an impermeable barrier to cross-fault flow, focusing fluid flow along the high permeability conduits created

https://doi.org/10.1017/S001675681000097X Published online by Cambridge University Press

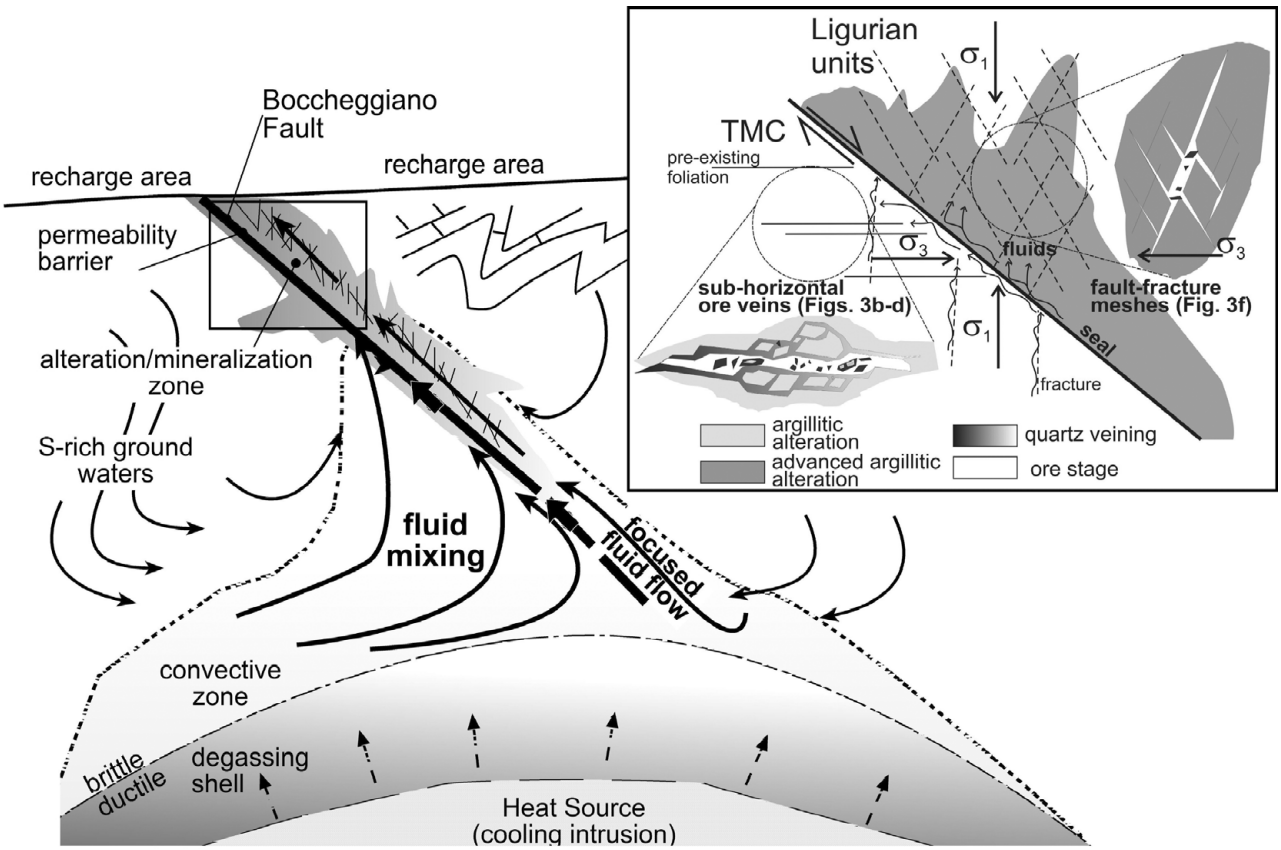

Figure 13. Conceptual model for the sulphide mineralization and hydrothermal outflow within the damage zone of the Boccheggiano Fault. The inset shows the different features of the structural permeability across the damage zone of the BF under the prevailing extensional stress regime accompanying sulphide mineralization (see text for further details).

at the fault hangingwall (Fig. 13). Interplay among active deformation, fracturing and sealing (e.g. Sibson, 1996; Cox, Knackstedt & Braun, 2001; Sheldon & Ord, 2005) during convective circulation at depth maintained by the cooling of the Montieri pluton was primarily responsible for the ore genesis along the hangingwall of the BF. Structural permeability at the fault hangingwall was achieved by means of a network of fault fracture meshes (cf. Sibson, 1996), compatible with the regional extensional stress field (see inset in Fig. 13). On the other hand, the extremely low permeability expected in the fault gouge was responsible for creation of forced fluid overpressure conditions (Neuzil, 1995; Sibson, 2000) at the footwall of the BF during fluid outflow at the fault hangingwall. This caused hydrofracturing of the country rocks below the seal created by the fault core, as attested by development of multiple episodes of sub-horizontal sulphide vein formation and brecciation. Formation of this vein swarm might have also been favoured by the pre-existing mechanical anisotropies (foliation planes) in the TMC rocks (see inset in Fig. 13). The higher homogenization temperatures derived from the fluid inclusions hosted in quartz from the footwall ore bodies of the BF together with the evidence of faulting post-dating ore formation suggest that footwall mineralization pre-dated the main ore genesis in the hangingwall. This argues that efficient fluid outflow along the BF occurred only after a threshold of critical fracture permeability (percolation threshold in Cox, Knackstedt & Braun, 2001) was overcome in the fault hangingwall. There, texture of the quartz crystals in the vein ores (Fig. 6f) argues that cyclic fluid supply accompanied ore genesis and that a cyclic fault valve behaviour (Sibson, 1992, 2004; Cox, 1995) may be invoked as a dynamic fluid flow model to create the fracture pathways for fluid percolation along the BF. During this upward flow, fluid immiscibility and polycyclic mineralization occurred, probably related to cyclically repeated pressure drops accompanying crack sealing during stress-induced dilatation and continuous deformation (e.g. Robert, Boullier & Firdaous, 1995). Fluid flow was further controlled by the relative permeability structure of the host rocks and fault zone elements, with fluid flow focused along the permeable/impermeable interfaces (cf. Rowland & Sibson, 2004). In the fault footwall, this process resulted in fluid flow focused along horizontal paths as documented by the multiple sub-horizontal skarn mineralization levels formed at the carbonate–phyllite interfaces (see inset in Fig. 2). Finally, degassing of the separated vapour phase occurred along the fracture conduits, forming steam-heated acid-sulphate waters and final weathering of the sulphide ores.

Even though this study presents analogies with the scenario reconstructed by Liotta *et al.* (2009),

https://doi.org/10.1017/S001675681000097X Published online by Cambridge University Press

important elements of novelty arise with elements that may contribute to refine conceptual models of fault hydraulic architecture in extensional settings. The major outcome of this study is that a large heterogeneity of fluid flow and hence of alteration/mineralization may be predicted across the damage zone of a major extensional fault zone. Particularly, hydraulic properties are strongly anisotropic when moving from the footwall to the hangingwall rocks, with fluid flow paths strongly influenced by (i) the fault core permeability (i.e. fault core thickness and grain size), and (ii) the anisotropic fracture permeability of the fault damage zone. In this context, the rate of secondary permeability creation and maintenance by active deformation in the hangingwall of the fault appears to be by far the major factor leading to effective hydraulic transmissivity in extensional terranes. Strongly focused fluid flow and structurally controlled mineralized zones are then expected within the fracture-controlled pathways created at the fault hangingwall.

The generalization of the model presented in this paper implies the prerequisite that, in extensional settings, hangingwall blocks are more deformed (and therefore likely more permeable) than footwall blocks. There is no definitive agreement in the current literature about whether asymmetric fault damage always occurs and localizes in the hangingwall of extensional faults, mostly because fault blocks often host deformations inherited from previous tectonic events and the deformation discrimination is usually difficult. However, modern technologies applied to actively deforming terranes have recently demonstrated that, in extensional settings, the fault hangingwall usually undergoes deformation larger than the fault footwall, as in the case of the April 2009 L'Aquila earthquake (magnitude 6.3) in central Italy (Walters *et al*. 2009; Wilkinson *et al*. 2010). Obviously, the contrast in the rheological properties between the hangingwall and footwall rocks may also play an important role in the finite deformation and damage (ductile versus brittle behaviour; cf. De Paola, Faulkner & Collettini, 2009) as may be the case in the BF, where foliated Palaeozoic phyllites are exposed at the footwall and Cretaceous marine siliceous–carbonate strata are exposed at the hangingwall.

10. Conclusions

This study documents that the bulk hydrological properties of the sulphide-mineralized fault damage zone of the BF were strongly influenced by the low permeability structure of the fault core, which induced fluid flow compartmentalization and dominant upward fault-parallel flow. Stress-controlled components of structural permeability created at the fault hangingwall enhanced bulk permeability and primarily controlled fluid outflow and mineralization, resulting in integrated fluid fluxes nearly one order of magnitude higher in the hangingwall than in the footwall. These features intimately link ore-grade mineralization in extensional settings to telescoping of hydrothermal flow along the fracture permeability in the hangingwall block(s) of major extensional fault systems.

Acknowledgements. This paper is dedicated to the memory of R. Funiciello, who promoted this research. We are indebted to T. Theye and A. Kazbor (Stuttgart University) for providing XRF data. The paper benefitted from constructive criticism from N. De Paola and advice from the journal editor M. Allen.

References

ARISI ROTA, F. & VIGHI, L. 1971. Le mineralizzazioni a pirite e a solfuri misti. *Rendiconti Società Italiana di Mineralogia & Petrografia*. **27**, 370–422.

ASPREY, L. B. 1976. The preparation of very pure fluorine gas. *Journal Fluorine Chemistry* **7**, 359–361.

BAKKER, R. J. 2003. Package FLUIDS 1. Computer programs for analysis of fluid inclusion data and for modelling bulk fluid properties. *Chemical Geology* **194**, 3–23.

BATINI, F., BROGI, A., LAZZAROTTO, A., LIOTTA, D. & PANDELI, E. 2003. Geological features of Larderello-Travale and Mt. Amiata geothermal areas (southern Tuscany, Italy). *Episodes* **26**, 239–44.

BELLANI, S., BROGI, A., LAZZAROTTO, A., LIOTTA, D. & RANALLI, G. 2004. Heat flow, deep temperatures and extensional structures in the Larderello geothermal field (Italy). Constraints on geothermal fluid flow. *Journal Volcanology Geothermal Research* **132**, 15–29.

BERTANI, R. 2005. World geothermal power generation in the period 2001–2005. *Geothermics* **34**, 65–690.

BERTINI, G., CASINI, G., GIANELLI, G. & PANDELI, E. 2006. Geological structure of the Larderello geothermal field. *Terra Nova* **18**, 163–9.

BILLI, A., VALLE, A., BRILLI, M., FACCENNA, C. & FUNICIELLO, R. 2007. Fracture-controlled fluid circulation and dissolutional weathering in sinkhole-prone carbonate rocks from central Italy. *Journal of Structural Geology* **29**, 385–95.

BODNAR, R. J. 1995. Fluid inclusion evidence for a magmatic source for metals in porphyry copper deposits. In *Magmas, Fluids and Ore Deposits* (ed. J. F. H. Thompson), pp. 139–52. Mineralogical Association of Canada, Short Course no. 23.

BODNAR, R. J. & VITYK, M. O. 1994. Interpretation of microthermometric data for H_2O–NaCl fluid inclusions. In *Fluid Inclusions in Minerals; Methods and Applications* (eds B. De Vivo & M. L. Frezzotti), pp. 117–30. Short Course of the IMA Working Group, Blacksburg, Virginia.

BOIRON, M. C., CATHELINEAU, M., RUGGIERI, G., JEANNINGROS, A., GIANELLI, G. & BANKS, D. A. 2007. Active contact metamorphism and CO_2–CH_4 fluid production in the Larderello geothermal field (Italy) at depths between 2.3 and 4 km. *Chemical Geology* **237**, 303–28.

BONS, P. D. 2000. The formation of veins and their microstructures. In *Stress, Strain and Structure, a Volume in Honour of W.D. Means* (eds M. W. Jessell & J. L. Urai). *Journal of the Virtual Explorer* **2**.

BOYCE, A. J., FULIGNATI, P. & SBRANA, A. 2003. Deep hydrothermal circulation in a granite intrusion beneath Larderello geothermal area (Italy): constraints from mineralogy, fluid inclusions and stable isotopes. *Journal of Volcanology and Geothermal Research* **126**, 243–62.

BROGI, A., LAZZAROTTO, A., LIOTTA, D. & RANALLI, G. 2003. Extensional shear zones as imaged by reflection

https://doi.org/10.1017/S001675681000097X Published online by Cambridge University Press

seismic lines; the Larderello geothermal field (central Italy). *Tectonophysics*, **363**, 127–39.

CAINE, J. S., EVANS, J. P., FORSTER & C. B. 1996. Fault zone architecture and permeability structure. *Geology* **24**, 1025–8.

CAMELI, G. M., DINI, I. & LIOTTA, D. 1993. Upper crustal structure of the Larderello geothermal field as a feature of post-collisional extensional tectonics, Southern Tuscany, Italy. *Tectonophysics* **224**, 413–23.

CARTWRIGHT, I. & BUICK, I. S. 1999. The flow of surface-derived fluids through Alice Springs age middle-crustal ductile shear zones, Reynolds Range, central Australia. *Journal of Metamorphic Geology* **17**, 397–414.

CATHELINEAU, M., MARIGNAC, C., BOIRON, M. C., GIANELLI, G. & PUXEDDU, M. 1994. Evidence of Li-rich brines and early magmatic water–rock interaction in a geothermal field: the fluid inclusion data from the Larderello field. *Geochimica Cosmochimica Acta* **58**, 1083–99.

CAVARRETTA, G., GIANELLI, G., & PUXEDDU, M. 1982. Formation of authigenic minerals and their use as indicators of the physicochemical parameters of the fluid in the Larderello-Travale geothermal field. *Economic Geology* **77**, 1071–84.

CLAYTON, R. N., O'NEIL, J. R. & MAYEDA, T. K. 1972. Oxygen isotope exchange between quartz and water. *Journal of Geophysical Research* **77**, 3057–67.

COELHO, J. 2006. GEOISO – A Windows™ program to calculate and plot mass balances and volume changes occurring in a wide variety of geologic processes. *Computers and Geosciences* **32**, 1523–8.

CORSINI, F., MORELLI, F. & TANELLI, G. 1991. A polymetallic sulfide (Cu–Pb–Zn) assemblage from the Boccheggiano-Campiano (Tuscany) pyrite deposit: application of the stannite–sphalerite geothermometer. *Neues Jahrbuch für Mineralogie, Monatshefte* **11**, 523–8.

CORTECCI, G., LATTANZI, P. & TANELLI, G. 1985. C- and O-isotope and fluid inclusion studies of carbonates from pyrite and polymetallic ore deposits and associated country rocks (southern Tuscany, Italy). *Chemical Geology* **58**, 121–8

COSTANTINI, A., ELTER, F. M., PANDELI, E., PASCUCCI, V. & SANDRELLI, F. 2002. Geologia dell'area di Boccheggiano e Serrabottini (Colline Metallifere, Toscana Meridionale) (with English abstract). *Bollettino della Società Geologica Italiana* **121**, 35–50.

COX, S. F. 1995. Faulting processes at high fluid pressures: an example of fault valve behavior from the Wattle Gully Fault, Victoria, Australia. *Journal of Geophysical Research* **100**, 12841–59, doi:10.1029/95JB00915.

COX, S. F., KNACKSTEDT, M. A. & BRAUN, J. 2001. Principles of structural control on permeability and fluid flow in hydrothermal systems. *Review in Economic Geology* **14**, 1–24.

CUREWITZ, D. & KARSON, J. A. 1997. Structural settings of hydrothermal outflow: fracture permeability maintained by fault propagation and interaction. *Journal of Volcanology and Geothermal Research* **79**, 149–68.

DAVIS, G. H. & REYNOLDS, S. J. 1996. *Structural Geology of Rocks and Regions*. New York: Wiley.

DE PAOLA, N., FAULKNER, D. R. & COLLETTINI, C. 2009. Brittle versus ductile deformation as the main control on the transport properties of low-porosity anhydrite rocks. *Journal of Geophysical Research* **114**, B06211, doi:10.1029/2008JB005967.

DINI, A. 2003. Ore deposits, industrial minerals and geothermal resources. *Periodico di Mineralogia* **72**, 41–52.

DINI, A., GIANELLI, G., PUXEDDU, M. & RUGGIERI, G. 2005. Origin and evolution of Pliocene–Pleistocene granites from the Larderello geothermal field (Tuscan Magmatic Province, Italy). *Lithos* **81**, 1–31.

DINI, A., INNOCENTI, F., ROCCHI, S., TONARINI, S. & WESTERMAN, D.S. 2002. The magmatic evolution of the late Miocene laccolith–pluton–dyke granitic complex of Elba Island, Italy. *Geological Magazine* **139**, 257–79.

DIPPLE, G. M. & FERRY, J. M. 1992. Metasomatism and fluid flow in ductile fault zones. *Contributions to Mineralogy and Petrology* **112**, 149–64.

EINAUDI, M. T., HEDENQUIST, J. W. & INAN, E. 2003. Sulfidation state of fluids in active and extinct hydrothermal systems: transitions from porphyry to epithermal environments. In *Volcanic, Geothermal, and Ore-Forming Fluids: Rulers and Witnesses of Processes Within the Earth* (eds S. F. Simmonds & I. Graham), pp. 285–314. Society of Economic Geologists, Special Publication no. 10.

FOURNIER, R. O. & POTTER, R. W. 1982. An equation correlating the solubility of quartz in water from 25° to 900°C at pressures up to 10,000 bars. *Geochimica Cosmochimica Acta* **46**, 1969–73.

FRANCESCHINI, F. 1998. Evidence of an extensive Pliocene-Quaternary contact metamorphism in Southern Tuscany. *Memorie della Società Geologica Italiana* **52**, 479–92.

FRANCUS, P. 1998. An image-analysis technique to measure grain-size variation in thin sections of soft clastic sediments. *Sedimentary Geology* **121**, 289–98.

FRIEDMAN, I. & O'NEIL, J. R. 1977. Compilation of stable isotope fractionation factors of geochemical interest. In *Data of Geochemistry, 6th edition* (ed. M. Fleischer). US Geological Survey Professional Paper 440-KK.

GIANELLI, G., MANZELLA, A. & PUXEDDU, M. 1997 Crustal models of the geothermal areas of southern Tuscany (Italy). *Tectonophysics* **281**, 221–39.

GIGGENBACH, W. F. 1992. Magma degassing and mineral deposition in hydrothermal systems along convergent plate boundaries. *Economic Geology* **97**, 1927–44.

GRANT, J. A. 1986. The isocon diagram a simple solution to Gresen's equation for metasomatic alteration. *Economic Geology* **81**, 1976–82.

HAAR, L., GALLAGHER, J. S. & KELL, G. S. 1984. NBS/NRC Steam Tables.

HANSON, R. B. 1995. The hydrodynamics of contact metamorphism. *Geological Society of America, Bulletin* **107**, 595–611.

HEDENQUIST, J. W. & LOWENSTERN, J. B. 1994. The role of magmas in the formation of hydrothermal ore deposits. *Nature* **370**, 519–27.

HEINRICH, C. A. 2005. The physical and chemical evolution of low-salinity magmatic fluids at the porphyry to epithermal transition: a thermodynamic study. *Mineralium Deposita* **39**, 864–89.

HENLEY, R. W. 1985. The geothermal framework of epithermal deposits. *Reviews in Economic Geology* **2**, 1–24.

JAGODZINSKI, H. 1949. Eindimensionale Fehlordnung in Kristallen Und ihr einfluss auf die röntgen interferenren. *Acta Crystallographica* **2**, 201–7.

JEFFERIES, S. P., HOLDSWORTH, R. E., WIBBERLEY, C. A. J., SHIMAMOTO, T., SPIERS, C. J., NIEMEIJER, A. R. & LLOYD, G. E. 2006. The nature and importance of

phyllonite development in crustal-scale fault cores: an example from the median tectonic line, Japan. *Journal of Structural Geology* **28**, 220–35.

JOLIVET, L., FACCENNA, C., GOFFÉ, B., MATTEI, M., ROSSETTI, F., BRUNET, C., STORTI, F., CADET, J. P., FUNICIELLO, R., D'AGOSTINO, N. & PARRA, T. 1998. Midcrustal shear zones in post-orogenic extension: example from the Northern Tyrrhenian Sea (Italy). *Journal of Geophysical Research* **103**, 12123–60.

KNIGHT, C. L. & BODNAR, R. J. 1989. Synthetic fluid inclusions: IX. Critical PVTX properties of NaCl-H_2O solutions. *Geochimica Cosmochimica Acta* **53**, 3–8.

LATTANZI, P. 1999. Epithermal precious metal deposits of Italy-an overview. *Mineralium Deposita* **34**, 630–8.

LIOTTA, D., RUGGIERI, G., BROGI, A., FULIGNATI, P., DINI, A. & NARDINI, I. 2009. Migration of geothermal fluids in extensional terrains: the ore deposits of the Boccheggiano-Montieri area (southern Tuscany, Italy). *International Journal of Earth Sciences* **99**, 623–44.

MARTARELLI, L., FERRINI, V. & MASI, U. 1995. Trace-element evidence for the genesis of the pyrite vein deposit of Campiano (southern Tuscany, Italy). *Periodico di Mineralogia* **64**, 349–66.

MASOTTI, A. & FAVILLI, G. 1987. Il giacimento di Campiano. *L'Industria Mineraria* **4**, 27–38.

MONGELLI, F., PIALLI, G. & ZITO, G. 1998. Tectonic subsidence, heat flow and uplift in Tuscany: a new geodynamic and geothermal approach. *Memorie della Società geologica Italiana* **52**, 275–82.

MOORE, D. E., HICKMAN, S., LOCKNER, D. A. & DOBSON, P.F. 2001. Hydrothermal minerals and microstructures in the Silangkitang geothermal field along the Great Sumatran fault zone, Sumatra, Indonesia. *Geological Society of America, Bulletin* **113**, 1179–92.

MOORE, D. M. & REYNOLDS, R. C. JR. 1997. *X-Ray Diffraction and the Identification and Analysis of Clay Minerals*. Oxford: Oxford University Press, 378 pp.

NEUZIL, C. E. 1995. Abnormal pressures as hydrodynamic phenomena. *American Journal of Science* **295**, 742–86.

OKAMOTO, A. & TSUCHIYA, N. 2009. Velocity of vertical fluid ascent within vein-forming fractures. *Geology* **37**, 563–6.

OLIVER, N. H. S. 1996. Review and classification of structural controls on fluid flow during regional metamorphism. *Journal of Metamorphic Geology* **14**, 477–92.

OLIVER, N. H. S. & BONS, P. D. 2001. Mechanisms of fluid flow and fluid–rock interaction in fossil metamorphic hydrothermal systems inferred from vein-wallrock patterns, geometry and microstructure. *Geofluids* **1**, 137–62.

OLIVER, N. H. S., RUBENACH, M. J., FU, B., BAKER, T., BLENKINSOP, T., CLEVERLEY, J. S., MARSHALL, L. J. & RIDD, P. J. 2006. Granite-related overpressure and volatile release in the mid crust: fluidized breccias from the Cloncurry District, Australia. *Geofluids* **6**, 346–58.

REYES, A. 1990. Petrology of Philippine geothermal systems and the application of alteration mineralogy to their assessment. *Journal of Volcanology and Geothermal Geology* **43**, 279–309.

RIMSTIDT, J. D. 1997. Quartz solubility at low temperatures. *Geochimica Cosmochimica Acta* **61**, 2553–8.

ROBERT, F., BOULLIER, A. M. & FIRDAOUS, K. 1995, Gold-quartz veins in metamorphic terranes and their bearing on the role of fluids in faulting. *Journal of Geophysical Research* **100**, 12861–79.

ROEDDER, E. 1984. *Fluid Inclusions*. Mineralogical Society of America, Reviews in Mineralogy 12.

ROSSETTI, F., BALSAMO, F., VILLA, I. M., BOUYBAOUENNE, M., FACCENNA, C. & FUNICIELLO, R. 2008. Pliocene-Pleistocene high-T/low-P metamorphism during multiple granitic intrusions in the southern branch of the Larderello geothermal field (Southern Tuscany, Italy). *Journal of the Geological Society, London* **165**, 247–62.

ROWLAND, J. V. & SIBSON, R. H. 2004. Structural controls on hydrothermal flow in a segmented rift system, Taupo Volcanic zone, New Zealand. *Geofluids* **4**, 259–83.

RUGGIERI, G., CATHELINEAU, M., BOIRON, M. C. & MARIGNAC, C. 1999. Boiling and fluid mixing in the chlorite zone of the Larderello geothermal system. *Chemical Geology* **154**, 237–56.

RUGGIERI, G. & GIANELLI, G. 1999. Multi-stage fluid circulation in a hydraulic fracture breccia of the Larderello geothermal field, Italy. *Journal of Volcanology and Geothermal Research* **90**, 241–61.

SHARP, Z. D. 1990. A laser-based microanalytical method for the in situ determination of oxygen isotope ratios of silicates and oxides. *Geochimica Cosmochimica Acta* **54**, 1353–7.

SHELDON, H. A. & ORD, A. 2005. Evolution of porosity, permeability and fluid pressure in dilatant faults post-failure: implications for fluid flow and mineralization. *Geofluids* **5**, 272–88.

SIBSON, R. H. 1987. Earthquake rupturing as a mineralizing agent in hydrothermal systems. *Geology* **15**, 701–4.

SIBSON, R. H. 1992. Implications of fault valve behaviour from rupture nucleation and recurrence. *Tectonophysics* **211**, 283–93.

SIBSON, R. H. 1996. Structural permeability of fluid-driven fault fracture meshes. *Journal of Structural Geology* **18**, 1031–42.

SIBSON, R. H. 2000. Fluid involvement in normal faulting. *Journal of Geodynamics* **29**, 469–99.

SIBSON, R. H. 2004. Controls on maximum fluid overpressure defining conditions for mesozonal mineralisation. *Journal of Structural Geology* **26**, 1127–36.

SIMMONS, S. F., WHITE, N. C. & JOHN, D. A. 2005. Geological characteristics of epithermal precious and base metal deposits. *Economic Geology, 100th Anniversary Volume*, pp. 485–522.

STERNER, S. M. & BODNAR, R. J. 1991. Synthetic fluid inclusions; X, Experimental determination of P-V-T-X properties in the CO_2 -H_2O system to 6 kb and 700°C. *American Journal of Science* **291**, 1–54.

STREIT, J. E. & COX, S. F. 1998. Fluid infiltration and volume change during mid-crustal mylonitization of Proterozoic granite, King Island, Tasmania. *Journal of Metamorphic Geology* **16**, 179–212.

TANELLI, G. 1983. Mineralizzazioni metallifere e minerogenesi della Toscana (with English abstract). *Memorie della Società Geologica Italiana* **25**, 91–109.

TITLEY, S. R. 1976. Evidence for a Mesozoic linear tectonic pattern in southeastern Arizona, Arizona. *Geological Society Digest* **10**, 71–101.

VELDE, B. 1985. Clay minerals, a physico-chemical explanation of their occurrence. *Developments in Sedimentology* **40**, 427.

VILLA, I. M., RUGGIERI, G., PUXEDDU, M. & BERTINI, G. 2006. Geochronology and isotope transport systematics in a subsurface granite from the Larderello-Travale geothermal system (Italy). *Journal of Geophysical Research* **152**, 20–50.

WALTERS, R. J., ELLIOTT, J. R., D'AGOSTINO, N., ENGLAND, P. C., HUNSTAD, I., JACKSON, J. A., PARSONS, B.,

PHILLIPS, R. J. & ROBERTS, G. 2009. The 2009 L'Aquila earthquake (central Italy): a source mechanism and implications for seismic hazard. *Geophysical Research Letters* **36**, L17312, doi:10.1029/2009GL039337.

WHITE, N. C. & HEDENQUIST, J. W. 1995. Epithermal gold deposits: styles, characteristics and exploration. *Society of Economic Geology Newsletter* **23**, 9–13.

WILKINSON, M., MCCAFFREY, K. J. W., ROBERTS, G., COWIE, P. A., PHILLIPS, R. J., MICHETTI, A. M., VITTORI, E., GUERRIERI, L., BLUMETTI, A. M., BUBECK, A., YATES, A., & SILEO, G. 2010. Partitioned postseismic deformation associated with the 2009 Mw 6.3 L'Aquila earthquake surface rupture measured using a terrestrial laser scanner. *Geophysical Research Letters* **37**, L10309, doi:10.1029/2010GL043099.

Appendix 1. Analytical methods

Fluid inclusion analyses

Microthermometric measurements have been carried out at the Flinc Lab of the Istituto di Geologia Ambientale e Geoingegneria, CNR, Rome, with a Linkam THMSG600 freezing/heating stage. The calibration of the stage was performed using pure natural CO_2 inclusions for low temperatures and synthetic fluid inclusions for high temperatures. Reproducibility of the triple point of CO_2 (T_{mCO_2}) at −56.6 °C was ± 0.2 °C (± 1 °C for heating runs). Eutectic and final melting temperatures (T_e and T_m, respectively) were determined with a 0.5–1 °C min^{-1} rate, homogenization temperature (T_h) with a heating rate of 5–10 °C min^{-1}.

Stable isotope analysis

Stable isotope ratios were measured at the Mass Spectrometry Lab of the Istituto di Geologia Ambientale e Geoingegneria, CNR, Rome. Mineral separation was achieved by hand picking. Oxygen isotope ratios of quartz samples were measured by laser fluorination (Sharp, 1990), reacting 1.5–1.8 mg fragments in a F_2 gas atmosphere. We employed a 15W CO_2 laser operating at a wavelength of 10.6 m to irradiate the samples, and pure fluorine desorbed at about 300 °C from hexafluoropotassium–nickelate salt (Asprey, 1976) as a reagent. The O_2 produced during laser fluorination was purified of excess fluorine and transferred to a cold finger with a 13 Å molecular sieve. Further oxygen gas purification was achieved by desorbing oxygen from the molecular sieve at around 110 °C using a liquid nitrogen–ethanol mixture. The purified gas was then transferred to a Finnigan Delta+ mass spectrometer for oxygen isotope analysis. The laboratory standard, calibrated against the NBS 28 standard, was measured several times during the analysis session. Its standard deviation after ten repetitions is less than 0.1. The oxygen isotope compositions are reported in the usual delta notation that represents the deviation in parts per million of the $^{18}O/^{16}O$ ratio relative the same ratio of the standard SMOW (Standard Mean Oceanic Water).

XRD analyses

XRD analyses were performed with a Scintag X_1 XRD system (CuKα radiation) at 40 kV and 45 mA at Roma Tre University. Randomly oriented whole-rock powders were run in the 2–70 °2θ interval with a step size of 0.05 °2θ and a counting time of 3 s per step. Oriented air-dried samples were scanned from 1 to 48 °2θ with a step size of 0.05 °2θ and a count time of 4 s per step. The presence of expandable clay minerals was determined for samples treated with ethylene glycol at room temperature for 24 hours. Ethylene glycol solvated samples were scanned at the same conditions as air-dried aggregates with a scanning interval of 1–30 °2θ. Expandability measurements for both I-S and C-S mixed-layer minerals were determined according to Moore & Reynolds (1997) using the delta two-theta method after decomposing the composite peaks between 9 and 10 °2θ and 16 and 17 °2θ for I-S and between 10 and 12.3 °2θ and 25 and 26 °2θ for C-S using Pearson VII functions. Peaks in relative close position were selected for clay mineral quantitative analysis of the <2 μm (equivalent spherical diameter) in order to minimize the angle-dependent intensity effect. Integrated peak areas were transformed into mineral concentrations by using mineral intensity factors as calibration constants (see Moore and Reynolds 1997 for a review). Non-clay minerals that were observed in the <2 μm grain-size fraction were not included in the quantitative analysis of the oriented aggregates, thus the given data refer to the phyllosilicate group only.

Whole-rock chemistry

Major and selected trace elements of bulk rock samples were measured by X-ray fluorescence analysis (XRF) with a Panalytical PW2400 sequential wavelength-dispersive X-ray spectrometer (equipped with a Rh excitation source) at the Institute of Mineralogy, University of Stuttgart. Glass discs were used for major elements, pressed powder pellets for trace elements. Calibration was done with international geochemical reference samples. The reproducibility was found to be smaller than 1 % for major elements and smaller than 2 % for trace elements. Loss on ignition (LOI) was determined by heating to 850 °C.

https://doi.org/10.1017/S001675681000097X Published online by Cambridge University Press